

Enhancing GNSS Water Vapour Retrieval via Synergistic Microwave Radiometry: Thermodynamic Error Diagnosis and Bias Correction

Avinash N. Parde¹, Christina Oikonomou¹, Haris Haralambous^{1,2}

¹Frederick Research Center, Nicosia, 1036, Cyprus

²Frederick University, Nicosia, 1036, Cyprus

Correspondence: Avinash N. Parde (res.pav@frederick.ac.cy)

Abstract.

The retrieval of Precipitable Water Vapour (PWV) from Global Navigation Satellite Systems (GNSS) in thermodynamically complex environments is significantly limited by the accuracy of the weighted mean temperature (T_m). This study evaluates the efficacy of static climatological models versus dynamic ground-based microwave radiometry for T_m determination in the Eastern Mediterranean, a region characterized by sharp refractivity gradients. Using the Cyprus GNSS Meteorology Enhancement research project (CYGMEN) infrastructure in Nicosia, the performance of the ERA5-based HGPT2 model and a co-located Microwave Radiometer (MWR) was assessed against radiosonde (RS) profiles during the 2025 warm season (Spring–Summer). Diagnostic analysis reveals that the static HGPT2 model fails to resolve the diurnal thermodynamic decoupling between the boundary layer and the free troposphere, leading to a systematic overestimation of T_m exceeding 6 K during peak solar insolation. Conversely, the MWR captures short-term thermodynamic variability ($r=0.98$) but exhibits a systematic cold bias of -1.91 K in raw retrievals. It is demonstrated that a site-specific linear bias correction reduces the MWR T_m Root Mean Square Error (RMSE) from 2.32 K to 1.43 K, significantly outperforming the empirical model. Sensitivity analysis confirms that thermodynamic uncertainty dominates the error budget, outweighing uncertainties in refractivity constants by an order of magnitude. Consequently, standard climatological retrievals diverge from the synergistic MWR-GNSS method during extreme hygrometric events, introducing systematic PWV biases exceeding 1.0 mm when moisture levels surpass 45 mm. The synergistic coupling of real-time radiometric T_m with GNSS data is therefore meaningful for generating climate-quality PWV records in semi-arid coastal regions.

1 Introduction

Atmospheric water vapour (WV) is the primary greenhouse gas, contributing approximately 60 % to the natural greenhouse effect and playing a vital role in regulating the Earth's thermodynamic budget (Kiehl and Trenberth, 1997; Trenberth et al., 2005). Furthermore, WV is the main driver of latent heat transport, influencing convective systems and global precipitation patterns. High-frequency variations in Precipitable Water Vapour (PWV) correlate strongly with atmospheric instability and are a key factor in the initiation of severe weather. Specifically, rapid temporal gradients in PWV often precede heavy rainfall

32 and flash floods, acting as a reliable precursor for convective storms (Brenot et al., 2013). Consequently, assimilating high-
33 resolution PWV data into Numerical Weather Prediction (NWP) models significantly improves short-range precipitation "now-
34 casting" (Bennitt and Jupp, 2012). Accurate PWV retrieval is especially crucial for the Eastern Mediterranean, a climate change
35 "hotspot" warming faster than the global average (Giorgi, 2006; Lelieveld et al., 2012). This region is characterized by complex
36 topography and land-sea contrasts, which create sharp atmospheric refractivity gradients. The Eastern Mediterranean faces a
37 hydro-climatic paradox: a long-term drying trend (-0.5 mm/decade) alongside increasing high-intensity, short-duration flash
38 flood events (Zittis et al., 2019; Ziv et al., 2021). GNSS-derived PWV in this region exhibits strong diurnal cycles with
39 amplitudes up to 5 mm, which are closely correlated with atmospheric instability (Ziskin Ziv et al., 2020). Despite this
40 vulnerability, the Eastern Mediterranean currently lacks dense, continuous atmospheric profiling networks. Traditional
41 observation methods, such as radiosondes (RS), fail to resolve these mesoscale events due to low temporal resolution (typically
42 12-hour intervals) and significant spatial gaps (Soden and Lanzante, 1996). While satellite-based passive remote sensing offers
43 global coverage, it is often limited by revisit times, daylight dependence, or data degradation in coastal zones due to land
44 contamination in the microwave footprint (Bennartz and Bauer, 2003).

45 These limitations underscore the necessity for ground-based remote sensing techniques that offer continuous, all-weather
46 operability. Ground-based Global Navigation Satellite Systems (GNSS) meteorology has emerged as a robust technique for
47 atmospheric sounding since the seminal proposal by Bevis et al. (1992). By estimating the Zenith Total Delay (ZTD) of GNSS
48 signals traversing the neutral atmosphere, the Zenith Wet Delay (ZWD) can be isolated by subtracting the Zenith Hydrostatic
49 Delay (ZHD), which is accurately modeled from surface pressure observations (Saastamoinen, 1972). GNSS-derived PWV
50 offers significant advantages, including high temporal resolution (sub-hourly), all-weather availability, and cost-efficiency by
51 leveraging existing geodetic infrastructure (Guerova et al., 2016; Jones et al., 2020).

52 The retrieval of PWV from GNSS ZWD relies on a dimensionless conversion factor, Π , which is a function of the
53 atmospheric weighted mean temperature, T_m . Defined physically as $\int(e/T)dz/\int(e/T^2)dz$ (Askne and Nordius, 1987), T_m
54 encapsulates the thermal state of the atmospheric column. Because the conversion factor (Π) is nearly linearly proportional to
55 T_m , any relative error in the T_m estimation strictly propagates as an equivalent relative error in the final PWV retrieval. During
56 severe moisture events with an PWV of 50 mm, this translates to an absolute error of ~ 0.18 mm. Consequently, a 1 % relative
57 error in T_m translates strictly to a 1 % relative error in PWV. Therefore, alongside the substantial errors inherent in ZTD
58 estimation—such as mapping function inaccuracies and surface pressure interpolation for the ZHD (Ning et al., 2016)—the
59 determination of T_m remains one of the primary sources of uncertainty in GNSS meteorology. In the absence of in-situ profiles,
60 T_m is commonly estimated using empirical regression models or global climatological models. However, earlier studies have
61 demonstrated that empirical T_m regressions, such as the Bevis model (Bevis et al., 1992), introduce relative PWV errors of 1–
62 2 % due to weak T_s – T_m correlations in coastal and equatorial regions, where annual/semiannual variations are not adequately
63 captured (Yao et al., 2014; Lan et al., 2016). Similarly, global grid-based T_m models like GPT2w achieve RMSE < 4 K at ~ 80

64 % of mid-latitude sites but degrade in data-sparse areas like the Middle East and Africa, where reanalysis quality is limited
65 (Böhm et al., 2015; Jiang et al., 2019). The Hourly Global Pressure and Temperature 2 (HGPT2) model represents a major
66 advancement by providing hourly estimates derived from ERA5 reanalysis (Mateus et al., 2021). Despite recent validation of
67 GPT2w and ECMWF models for Precipitable Water Vapour (PWV) retrieval in the Mediterranean (Oikonomou et al. 2018),
68 a critical gap exists: the quantification of vertical interpolation errors in these models, especially over complex coastal terrains.
69 For instance, while recent validation studies in Cyprus demonstrate strong GNSS-PWV correlations (>0.6) with ERA5 during
70 extreme precipitation, persistent reanalysis interpolation errors are highlighted in mountainous areas (Giannadaki et al., 2025).
71 This lack of validation for HGPT2's performance in the complex topography of the Eastern Mediterranean potentially
72 exacerbates PWV biases during extreme events.

73 An alternative approach to deriving T_m is the use of ground-based Microwave Radiometers (MWR). MWRs measure
74 brightness temperatures at multiple frequencies to retrieve continuous vertical profiles of temperature and humidity. Ground-
75 based MWRs have been shown to retrieve T_m with RMSE $\sim 1\text{--}2$ K in mid-latitudes, outperforming empirical models during
76 synoptic anomalies (Cimini et al., 2010; Crewell and Löhnert, 2007; Löhnert et al., 2012). While multi-site intercomparisons
77 reveal that MWR retrievals can exhibit upper-tropospheric cold biases (up to 5 K at >2 km altitude) (Van Malderen et al.,
78 2014; Steinke et al., 2015), simple linear corrections can reduce RMSE by 20–40 % (Ning and Elgered, 2021). Operational
79 GNSS–MWR synergies for T_m bias correction have documented gains in PWV accuracy (10–30 % RMSE reduction) in
80 European networks (Vaquero-Martínez et al., 2018; Li et al., 2020). However, such applications are rare in the semi-arid
81 Eastern Mediterranean, where MWR could critically mitigate reanalysis uncertainties.

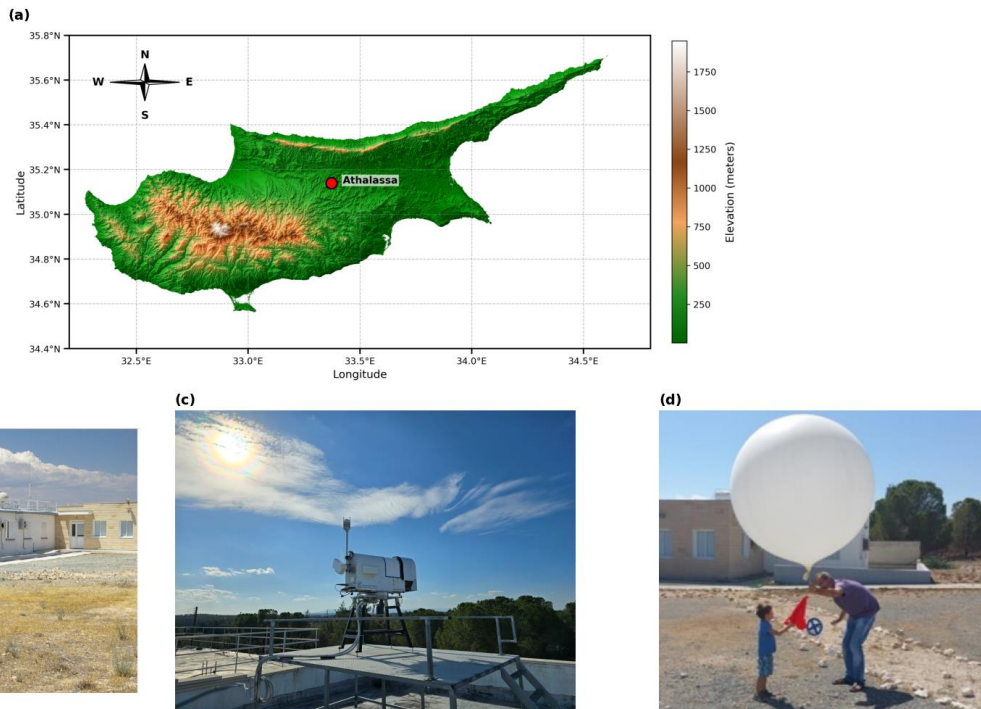
82 This study leverages the infrastructure of the CYGMEN (Cyprus GNSS Meteorology Enhancement) project, which is
83 establishing a dense, multi-sensor meteorological network in Cyprus. The network, termed CyMETEO, integrates a dense
84 array of continuous GNSS stations distributed across the island. Due to the high cost and operational complexity of radiometric
85 profiling, the network currently features a single, centralized thermodynamic 'supersite' at the Athalassa observatory, where a
86 GNSS receiver is strictly co-located with a MWR and a RS launch facility. This unique instrumental setup provides an ideal
87 testbed for inter-comparing atmospheric retrieval techniques in a coastal, semi-arid environment. The primary objective of this
88 manuscript is to evaluate the accuracy of GNSS-derived PWV over the Eastern Mediterranean by assessing the performance
89 of different T_m determination strategies. We specifically investigate the efficacy of the HGPT2 model compared to MWR-
90 derived T_m and RS benchmarks. The study aims to quantify the error budget of GNSS-PWV and determine whether the
91 inclusion of MWR data provides statistically significant improvements over the state-of-the-art HGPT2 model. The manuscript
92 is organized as follows: Section 2 describes the study area and the instrumentation of the CyMETEO network; Section 3 details
93 the methodology for GNSS processing, ZTD estimation, and the mathematical derivation of T_m from different sources; Section
94 4 presents the validation results and statistical analysis against RS reference data; and Section 5 concludes with
95 recommendations for operational PWV monitoring strategies in the region.

96

97 **2 Data and Methodology**

98 **2.1 Observational Site and CYGMEN Infrastructure**

99 The observational campaign was conducted at the Athalassa atmospheric observatory in Nicosia, Cyprus (35.15°N, 33.40°E,
 100 160 m a.s.l.), situated in the central Mesaoria plain. The site is characterized by complex topography, bounded by the Troodos
 101 Mountain to the southwest and the Pentadaktylos Mountain to the north, as shown in Fig. 1a. This study presents the first
 102 comprehensive analysis of radiometric data acquired under the CYGMEN infrastructure project, established to monitor the
 103 thermodynamic state of the Eastern Mediterranean atmosphere. To ensure robust thermodynamic profiling and validation,
 104 three primary datasets were collated, as shown in Table 1:



105 **Figure 1.** Location and instrumentation at Athalassa, Cyprus. (a) Site location on the island's elevation map. (b) GNSS reference station.
 106 (c) RPG-HATPRO radiometer. (d) Radiosonde balloon launching.
 107

108

109 **Table 1:** Summary of Instrumentation and Datasets

Parameter	Microwave Radiometer (MWR)	Radiosonde (RS)	GNSS Station
Instrument Model	HATPRO-Gen5 (RPG)	Vaisala RS41-SGP	GNSS Receiver LEICA GR50 (Collocated)
Role in Study	Synergistic thermodynamic profiling (temperature and humidity) and PWV estimation	<i>In-situ</i> "Ground Truth" Reference	ZTD Source for PWV Retrieval

Observation Type	Passive remote sensing (22–58 GHz)	<i>In-situ</i> vertical profile (balloon-borne)	Continuous satellite signal delay
Key Variables	Brightness Temp (T_B), $T(z)$, $\rho_v(z)$, PWV	$P(z)$, $T(z)$, $RH(z)$, Geopotential Height	Zenith Total Delay (ZTD)
Vertical Range	Surface to 10 km (94 levels)	Surface to burst altitude (~30 km)	Column-integrated (single value)
Temporal Resolution	High frequency (~1 s raw, resampled to 15 min)	Periodic (launch dependent)	Continuous (high rate)
Accuracy / Noise	T_B noise < 0.11 K (K-band), < 0.32 K (V-band)	T : 0.3 K, RH : 4 % (Manufacturer spec)	ZTD precision ~mm level
Auxiliary Data	Vaisala WXT536 (Rain, Surface Met)	GPS position/height	Surface Pressure

110

111 2.2 Instrumentation and Data Processing

112 2.2.1 Microwave Radiometry (MWR)

113 The RPG-HATPRO radiometer observes downwelling atmospheric brightness temperatures (T_B) across 14 channels: seven in
114 the K-band (22–31 GHz) sensitive to water vapour, and seven in the V-band (51–58 GHz) sensitive to oxygen for temperature
115 profiling. This instrument enables the continuous retrieval of temperature (T) and absolute humidity (ρ_v) profiles on a
116 standardized grid of 94 vertical levels from the surface up to 10 km. The vertical resolution is optimized for the planetary
117 boundary layer (PBL), ranging from 10–30 m up to 500 m, and decreasing to 100–500 m in the free troposphere. For this
118 study, high-frequency MWR observations were resampled to 15-minute intervals to align with GNSS processing epochs. It is
119 a well-documented limitation of passive microwave radiometry that retrieval accuracy degrades significantly during
120 precipitation, as liquid water on the instrument's radome heavily contaminates the measured brightness temperatures (Foth et
121 al., 2024; Parde et al., 2025; Pakkattil et al., 2025; Ware et al., 2004). Because this study focused on the warm, dry season in
122 the Eastern Mediterranean (March–October 2025), rainfall events were naturally sparse. Nevertheless, to ensure data integrity,
123 real-time precipitation flags generated by the co-located Vaisala WXT536 surface weather transmitter were utilized as a strict
124 quality-control filter. Any MWR profiles retrieved during active precipitation events were excluded from the dataset to prevent
125 wet-radome anomalies from artificially skewing the thermodynamic bias analysis. To diagnose potential biases in the MWR-
126 derived T_m , the dataset was split into a training Set (April–June 2025) for regression modeling and a validation Set (July–
127 October 2025) for independent testing. In addition to thermodynamic profiling, the MWR's native retrieval algorithm possesses
128 the capacity to directly estimate PWV from its K-band brightness temperatures.

129 Any MWR profiles retrieved during active precipitation events were excluded from the dataset to prevent wet-radome
130 anomalies from artificially skewing the thermodynamic bias analysis. To mitigate T_m errors in MWR, a supervised linear

131 regression model was developed to calibrate the MWR observations. For robust independent validation, the collocated dataset
 132 was separated into two distinct temporal subsets: the training Set (April – June 2025), which was used to derive the regression
 133 coefficients, and the validation Set (July – October 2025), which was used exclusively to test the correction's performance on
 134 unseen data. A simple linear correction model was fitted to the training data using Ordinary Least Squares (OLS) minimization.
 135 The relationship is defined in Eq. (1) as:

$$136 \quad T_{m,corr} = \alpha \cdot T_{m,MWR} + \beta \quad (1)$$

137 where $T_{m,corr}$ is the corrected MWR temperature, $T_{m,MWR}$ is the raw T_m derived from the radiometer and α (slope) and β
 138 (intercept) are the learned coefficients minimizing the residual sum of squares between the MWR and RS values. Based on
 139 our training Set, the derived coefficients applied to the validation Set were $\alpha = 1.0623$ and $\beta = -15.6062$ K. In addition to
 140 thermodynamic profiling, the MWR's native retrieval algorithm possesses the capacity to directly estimate PWV from its K-
 141 band brightness temperatures.

142

143 2.2.2 Radiosonde Data Processing

144 To establish a rigorous validation dataset, PWV was derived from high-resolution vertical profiles obtained from collocated
 145 radiosonde launches. A strict collocation window was applied, where MWR profiles were averaged within ± 30 minutes of the
 146 balloon launch time. The raw telemetry data, comprising pressure (P), temperature, and dew point temperature (T_d), were
 147 processed to derive the total columnar water vapour content (in kg m^{-2}) through the vertical integration of specific humidity,
 148 assuming the atmosphere is in hydrostatic equilibrium. The determination of the necessary moisture variables relied on the
 149 Magnus-Tetens approximation, which provides a widely accepted empirical relationship for saturation vapour pressure. First,
 150 the actual vapour pressure (e , in hPa) was computed directly from the dew point temperature (T_d , in $^{\circ}\text{C}$). This calculation
 151 utilized the coefficients defined by Bolton (1980), which are optimized for saturation vapour pressure over liquid water in the
 152 meteorological temperature range, as shown in Eq. (2):

$$153 \quad e = 6.112 \cdot \exp\left(\frac{17.67 \cdot T_d}{T_d + 243.5}\right) \quad (2)$$

154 Subsequently, the specific humidity (q , in kg kg^{-1}) was derived via Eq. (3), representing the mass mixing ratio of water vapour
 155 to the total moist air parcel:

$$156 \quad q = \frac{\epsilon \cdot e}{P - (1 - \epsilon) \cdot e} \quad (3)$$

157 where P is the static pressure (hPa) and $\epsilon \approx 0.622$ represents the ratio of the molecular weight of water vapour to that of dry
 158 air. Once the specific humidity profile was established, the PWV was calculated by integrating q with respect to pressure. The
 159 retrieval algorithm employed the trapezoidal rule for numerical integration, which approximates the integral as the sum of
 160 discrete atmospheric layers (Eq. 4):

$$161 \quad IWW = \frac{1}{g} \sum_{i=0}^{N-1} \frac{q_i + q_{i+1}}{2} \cdot |P_{i+1} - P_i| \quad (4)$$

162 where g is the gravity dependent on altitude, $g(\phi, h)$, where ϕ represents the Geodetic latitude and h is the orthometric height.
163 P is converted to Pascals (Pa) prior to integration and N represents the total number of vertical levels in the RS profile. It
164 should be noted that while the trapezoidal rule can theoretically overestimate the integral of an exponentially decaying profile,
165 the Vaisala RS41-SGP provides high-frequency 1-second telemetry (yielding a vertical spatial resolution of approximately 5
166 to 8 meters). At this exceptionally fine resolution, the linear approximation between measurement levels effectively converges
167 with the true atmospheric profile, rendering any systematic integration bias mathematically negligible. Also, it should be noted
168 that IWV, representing the mass column integral in kg m^{-2} , is physically and numerically equivalent to PWV expressed as a
169 depth in millimeters (mm), assuming the standard density of liquid water (1000 kg m^{-3}). A strict quality assurance protocol
170 was implemented to ensure vertical completeness; only radiosonde flights that successfully maintained continuous telemetry
171 up to the 10 km AGL integration ceiling were included in the final comparative dataset. While the term PWV is frequently
172 used when discussing direct profile integration from the MWR and RS, this study uses PWV (mm) as the standardized final
173 retrieval metric to align with operational meteorological and forecasting conventions. It is important to note that while the
174 nominal manufacturer uncertainty for the Vaisala RS41 humidity sensor is stated as 4 % for individual profile measurements,
175 the uncertainty of the resulting PWV is significantly lower. Because PWV is computed by integrating hundreds of discrete
176 measurements across the vertical column (Eq. 3), uncorrelated random sensor noise is largely suppressed through statistical
177 cancellation. Consequently, the integrated variables derived from the radiosonde, such as PWV and the T_m , possess the requisite
178 precision to serve as a robust 'ground truth' standard for evaluating the finer relative uncertainties (1–2 %) associated with the
179 GNSS and MWR retrievals. To ensure a rigorous and direct intercomparison with the active MWR, the radiosonde integration
180 was strictly confined to a maximum altitude of 10 km Above Ground Level (AGL). This vertical cutoff was deliberately chosen
181 to exactly match the 10 km ceiling of the standard RPG-HATPRO retrieval grid. While GNSS integrates delays through the
182 entire atmosphere, bounding the in-situ reference data is mathematically necessary to isolate profiling performance. It is well
183 established that this 10 km threshold does not introduce a systematic dry bias when comparing against total-column GNSS
184 (Van Baelen et al., 2005). Furthermore, ambient temperatures at this altitude range from $-40 \text{ }^\circ\text{C}$ to $-50 \text{ }^\circ\text{C}$, strictly limiting the
185 saturation vapour pressure. Consequently, the residual water vapour between 10 km and the tropopause is thermodynamically
186 constrained to fractions of a millimeter. Omitting this minute residual mass is functionally negligible, as it falls well within
187 the overall baseline uncertainty (typically 1–2 mm) of the total-column radiosonde PWV retrieval.

188

189 **2.2.3 GNSS Data Processing**

190 ZTD estimates were derived from the collocated Leica GR50 receiver (station NICO) using the Tefnut PP software (Douša et
191 al., 2014). The processing employed a Precise Point Positioning (PPP) strategy with an elevation cutoff angle of 10° . To
192 account for tropospheric mapping errors, the Vienna Mapping Function 1 (VMF1) was applied. Station coordinates were
193 constrained to the IGS14 reference frame, and satellite orbits and clock corrections were utilized from IGS Ultra-Rapid
194 products. While IGS Final products are the gold standard for historical climate reprocessing due to their minimal orbital

195 uncertainty, this study deliberately utilized IGS Ultra-Rapid products to evaluate the proposed synergistic retrieval architecture
 196 under near real-time operational constraints. Because a primary application of continuous GNSS-PWV is its assimilation into
 197 short-range NWP for severe weather 'nowcasting', it is crucial to assess system performance using the satellite orbits and clocks
 198 actually available during active forecasting. Although Ultra-Rapid products introduce a slight degradation in ZTD precision
 199 compared to final products, this uncertainty (typically fractions of a millimeter in PWV) remains negligible compared to the
 200 massive, multi-millimeter systematic errors introduced by static thermodynamic modeling, which is the primary focus of this
 201 investigation. While modern Numerical Weather Prediction systems frequently assimilate ZTD directly to avoid conversion
 202 uncertainties, deriving an accurate physical PWV product remains essential. PWV serves as an intuitive, absolute moisture
 203 metric heavily utilized by operational forecasters for severe weather nowcasting, and is fundamentally necessary for building
 204 long-term, cross-instrument climatological records. To isolate the ZWD, the ZHD was precisely calculated using continuous,
 205 co-located surface pressure observations obtained directly from the Vaisala WXT536 weather transmitter installed at the site,
 206 rather than relying on interpolated pressure fields. ZTD values were estimated at 15-minute intervals, directly aligning with
 207 the temporal resolution of the MWR. It must also be noted that the computation of ZHD is significantly dependent on the
 208 assumed value of the dry refractivity constant, k_1 . As established by Bevis et al. (1994) and further evaluated by Healy (2011),
 209 while k_1 is known to a high degree of relative accuracy, its residual fractional uncertainty introduces a persistent systematic
 210 bias into the ZHD estimation. Because ZWD is isolated by subtracting ZHD from the total delay, this k_1 -induced bias directly
 211 propagates into the final PWV error budget, acting alongside the conversion uncertainties analyzed later in this study.

212

213 **2.3 Thermodynamic Modeling and Synergistic Retrieval Strategy**

214 The conversion of GNSS-derived ZWD to PWV is governed by a proportionality factor, Π , whose accuracy is largely dictated
 215 by the T_m . To assess the fidelity of thermodynamic inputs for GNSS meteorology, we evaluated three distinct T_m derivation
 216 strategies. For profile-resolving instruments (MWR and RS), T_m values were computed by integrating the vertical profiles of
 217 physical temperature, $T(z)$ (K), and absolute humidity, $\rho_v(z)$ (kg m^{-3}). Consistent with Bevis et al. (1992), T_m is defined as the
 218 mean temperature of the atmosphere weighted by the water vapour partial pressure, which can be expressed in terms of vapour
 219 density as shown in Eq. (5):

$$220 \quad T_m = \frac{\int_{z_{surf}}^{z_{top}} \rho_v(z) dz}{\int_{z_{surf}}^{z_{top}} \frac{\rho_v(z)}{T(z)} dz} \quad (5)$$

221 In practice, the continuous integrals were discretized using the trapezoidal rule from the surface (z_{surf}) to the highest available
 222 profile level (z_{top}). This approach assumes linear variation of T and ρ_v between measurement levels. For standalone GNSS
 223 retrieval (where no dynamic profiles are available), T_m was derived from the HGPT2 (Hourly Global Pressure and Temperature
 224 2) model (Mateus et al., 2021). HGPT2 is an advanced 'blind' empirical model, meaning its outputs are independent of the
 225 specific observational year. While dynamic NWP models provide superior real-time meteorological data, 'blind' models like

226 HGPT2 remain heavily utilized in standard geodetic GNSS processing where real-time meteorological or NWP data streams
 227 are unavailable. It is constructed from a comprehensive 20-year historical baseline of atmospheric data from the ERA5 global
 228 reanalysis. Unlike standard static climatologies, HGPT2 leverages the full ERA5 spatial resolution (0.25°×0.25°) and provides
 229 temporal resolution at 1-hour intervals for any given Day of Year (DOY). It achieves this by employing a time-segmentation
 230 concept, modeling thermodynamic variables via long-term mean values combined with annual, semi-annual, and quarterly
 231 periodic functions.

232 Applying the linear correction model (as formulated in Section 2.2.1) successfully re-centers the error distribution. To quantify
 233 the benefits of sensor synergy in integrated water vapour estimation, this study defines and contrasts two distinct GNSS PWV
 234 retrieval architectures. The first, “Standard Retrieval” which is a control method utilizes the ZTD_{GNSS} combined with the T_m
 235 derived empirically from the HGPT2 climatological model (Böhm et al., 2015). Second “Synergistic Retrieval” which
 236 proposed method couples ZTD_{GNSS} with a physical T_m derived directly from a collocated MWR. For the synergistic approach,
 237 the dimensionless conversion factor (Π) was calculated dynamically using the MWR-derived T_m following Eq. (6) and Eq. (7).

$$238 \quad PWV = \Pi \cdot ZWD \quad (6)$$

$$239 \quad \Pi = \frac{10^6}{\rho_w R_v [k_2' + (k_3/T_m)]} \quad (7)$$

240
 241 where ρ_w represents the density of liquid water (1000 kg m⁻³) and R_v is the specific gas constant for water vapour (461.52 J
 242 kg⁻¹K⁻¹). To assess the sensitivity of the Π to the choice of thermodynamic coefficients, three widely used formulations were
 243 employed in this study, following Davis (1985)/Thayer (1974), Bevis et al. (1994), and Rüeiger (2002), as shown in Table 2:

244 **Table 2.** Refractivity constants used in the sensitivity analysis of the Π factor, based on three commonly adopted formulations.

Method	k_2 (K hPa ⁻¹)	k_3 (K ² hPa ⁻¹)	k_2' (K hPa ⁻¹)
Davis (1985) / Thayer (1974)	64.79	3.776×10 ⁵	16.52
Bevis et al. (1994)	70.40	3.739×10 ⁵	22.13
Rüeiger (2002)	71.295	3.7546×10 ⁵	22.97

245
 246 To rigorously quantify the uncertainty in the final PWV retrieval and avoid fragmented error attributions, standard error
 247 propagation must be applied to the fundamental conversion Eq. 6. Assuming the uncertainties in the wet delay and the
 248 conversion factor are uncorrelated, the variance of the final PWV (σ_{PWV}^2) is expressed using partial derivatives as in Eq. (8):

$$249 \quad \sigma_{PWV}^2 = \left(\frac{\partial PWV}{\partial ZWD}\right)^2 \sigma_{ZWD}^2 + \left(\frac{\partial PWV}{\partial \Pi}\right)^2 \sigma_{\Pi}^2 \quad (8)$$

250 Evaluating these primary partial derivatives yields the proportional contributions of the geodetic and thermodynamic
 251 components as shown in Eq. (9):

$$252 \quad \sigma_{PWV}^2 = \pi^2 \sigma_{ZWD}^2 + ZWD^2 \sigma_{\pi}^2 \quad (9)$$

253 The uncertainty in the conversion factor (σ_{π}^2) is itself a compound term driven by the T_m and the static atmospheric refractivity
 254 constants (k_2' and k_3). Its variance is defined via partial derivatives as shown in Eq. (10):

$$255 \quad \sigma_{\pi}^2 = \left(\frac{\partial \pi}{\partial T_m} \right)^2 \sigma_{T_m}^2 + \left(\frac{\partial \pi}{\partial k_2'} \right)^2 \sigma_{k_2'}^2 + \left(\frac{\partial \pi}{\partial k_3} \right)^2 \sigma_{k_3}^2 \quad (10)$$

256 The sensitivity of the conversion factor strictly to T_m (the dynamic thermodynamic variable evaluated in this study) is quantified
 257 by its partial derivative and it represented as Eq. (11):

$$258 \quad \frac{\partial \pi}{\partial T_m} = \pi \left[\frac{k_3}{T_m^2 (k_2' + \frac{k_3}{T_m})} \right] \quad (11)$$

259 This consolidated formulation establishes the exact mathematical limits of thermodynamic error propagation. As demonstrated
 260 in the sensitivity analysis (Section 3.4), this framework accurately isolates the dynamic uncertainties driven by T_m from the
 261 baseline static biases introduced by the chosen refractivity constants.

262

263 **2.4 Diagnostic Parameters and Error Analysis**

264 The vertical structure of the atmosphere was analyzed by segregating the dataset into two regimes: the PBL (0-2 km), where
 265 water vapour is concentrated, and the Free Troposphere (> 2 km). Additionally, the water vapour scale height (H_v) was
 266 calculated to parameterize the vertical distribution of moisture. H_v was derived for both RS and MWR by fitting an exponential
 267 decay function (Eq. 12) to the absolute humidity profile (ρ_v).

$$268 \quad \rho_v(z) = \rho_{v,0} \cdot \exp\left(-\frac{z}{H_v}\right) \quad (12)$$

269 where $\rho_v(z)$ is the absolute humidity at height z , and $\rho_{v,0}$ is the surface humidity. This curve fitting was deliberately restricted
 270 to the lowest 4 km of the atmosphere. Because this layer contains the vast majority (>90%) of the tropospheric water vapour
 271 mass, bounding the fit prevents the algorithm from heavily weighting near-zero, noisy upper-tropospheric values that
 272 mathematically degrade the fit for the boundary layer. Furthermore, the scale height metric fundamentally assumes the
 273 atmosphere conforms to a well-behaved exponential decay. Profiles yielding H_v values outside the physically realistic range
 274 of 0.1 to 4.0 km were excluded from the statistical analysis to prevent artificial statistical skewing during complex
 275 meteorological states (e.g., deep convective mixing) where the underlying exponential model is invalid. Forcing a
 276 mathematical fit onto these non-exponential profiles yields physically meaningless artifacts. Therefore, a Quality Assurance
 277 filter was applied, bounding the analysis to the physically realistic range of $0.1 \text{ km} < H_v < 4.0 \text{ km}$. Profiles yielding values
 278 outside this range were discarded because they indicate the underlying exponential model itself is invalid for that specific
 279 atmospheric profile, preventing artificial statistical skewing in the instrument intercomparison. Profiles yielding H_v values
 280 outside the physically realistic range of 0.1 to 4.0 km were excluded from the statistical analysis. To evaluate the performance

281 limitations of standard climatological models under varying hygrometric conditions, the systematic error (ΔPWV) was defined
282 as the residual between the synergistic and standard approaches (Eq. 13):

$$283 \quad \Delta PWV = PWV_{Synergistic} - PWV_{Standard} \quad (13)$$

284 The dataset was stratified into discrete bins of 5 mm PWV to isolate regimes of moisture abundance. Within each bin, the
285 mean bias and $\pm 1\sigma$ uncertainty were computed. These statistics were utilized to determine the "Systematic Bias Threshold,"
286 defined herein as the specific hygrometric threshold where the systematic model error exceeds 1 mm. Finally, the propagation
287 of thermodynamic uncertainty into the moisture retrieval was quantified via linear regression analysis. This compared the
288 relative error in T_m (HGPT2 vs. MWR) against the resulting relative error in PWV, serving as an empirical verification of the
289 theoretical sensitivity approximation given in Eq. (14):

$$290 \quad \frac{\Delta PWV}{PWV} \approx \frac{\Delta T_m}{T_m} \quad (14)$$

291 **3 Results**

293 The following evaluation follows a top-down diagnostic approach. First, the macroscopic baseline performance of the final
294 derived moisture products is established. Subsequently, the underlying thermodynamic variables driving these discrepancies
295 are isolated, culminating in the development of a targeted calibration scheme to mitigate the identified biases.

296 **3.1 Temperature and Humidity Profile Validation**

297 MWR-retrieved temperature T and ρ_v profiles were validated against collocated RS observations at 00:00 UTC and 12:00 UTC
298 during March–October 2025. Profiles were stratified into the planetary boundary layer (PBL; 0–2 km) and free troposphere
299 (>2 km), as shown in Figs. 2 and 3. Mean vertical temperature profiles show agreement between MWR and RS (Fig. 2a–b).
300 In the boundary layer (0–2 km), MWR retrieves temperature with high precision ($r > 0.98$, $RMSE < 1.5$ K). Above 2 km, a cold
301 bias is observed in the MWR retrieval, reaching -5.16 K at 12 UTC (Fig. 2f). Despite this bias, the linearity remains strong
302 ($r \approx 0.97$), indicating the sensor captures relative thermal variations aloft despite the absolute offset. This confirms the trend
303 observed in the mean profiles, where the MWR underestimates temperatures in the mid-to-upper troposphere. Furthermore,
304 horizontal balloon drift driven by prevailing winds inevitably causes the radiosonde to sample a different atmospheric volume
305 than the MWR's strict zenith view. While this spatiotemporal mismatch introduces random scatter into the upper-level
306 comparisons, it does not artificially skew the systematic biases identified in this study. Consequently, the RMSE increases
307 substantially to approximately 6.4 – 6.7 °C. The stark contrast in accuracy between the lower and upper troposphere is a known
308 characteristic of ground-based microwave radiometry (Parde et al., 2025; Pakkattil et al., 2025). The high accuracy below 2
309 km is attributed to the high information content of the opaque V-band channels (51–58 GHz), whose weighting functions peak
310 near the surface. Above 2 km, these weighting functions broaden significantly, reducing vertical resolution and causing a

311 "smearing" effect where the instrument provides a volume-averaged temperature rather than a precise point measurement. The
312 observed cold bias is likely a result of the retrieval algorithm (e.g., neural network) relying heavily on a climatological *a priori*
313 dataset that does not perfectly represent the thermal conditions of the transition season observed, or systematic offsets in the
314 radiative transfer model (absorption coefficients) used for training.

315 The mean ρ_v profiles (Figs. 3a–b) show the expected exponential decrease of moisture with height. At 00 UTC, the profiles
316 align reasonably well. However, at 12 UTC, the MWR profile exhibits a structural deviation between 1–2 km, failing to capture
317 the smooth moisture gradient recorded by the RS. This discrepancy may be attributed to the MWR's limited vertical resolution
318 during periods of active daytime mixing or complex humidity layering. The retrieval of humidity in the lower atmosphere
319 shows moderate agreement but is less accurate than the temperature retrievals. Performance is notably better at night (00 UTC)
320 with r of 0.878 and RMSE of 1.98 g m^{-3} . At 12 UTC, the correlation drops to 0.744, and the scatter increases (RMSE = 2.31 g
321 m^{-3}). Because the integrated mass of the water vapour column is physically and numerically equivalent to its depth (assuming
322 the standard density of liquid water), this physical quantity is exclusively referred to as PWV expressed in millimeters (mm)
323 throughout this study to align with operational meteorological conventions. A negative bias persists at both times (-0.51 g m^{-3}
324 at 00 UTC and -0.91 g m^{-3} at 12 UTC), indicating a tendency for the MWR to underestimate moisture content in the boundary
325 layer, particularly during the day. Surprisingly, the statistical linearity for ρ_v improves slightly or remains stable above 2 km,
326 likely due to the lower overall magnitude of humidity at these heights. The correlation coefficients remain stable (~ 0.87). In
327 contrast to the lower levels, the bias shifts to slightly positive values (0.23 g m^{-3} at 00 UTC and 0.46 g m^{-3} at 12 UTC),
328 suggesting a slight moist bias in the MWR retrievals aloft. The linear fits (Figs. 3e–f) align closely with the 1:1 line, with
329 slopes near unity (0.90 and 1.00), indicating that the MWR effectively captures the free tropospheric humidity trends despite
330 the lower absolute values. The difficulty in retrieving accurate ρ_v profiles, particularly at 12 UTC, stems from the limited
331 vertical resolution of the K-band channels (22–31 GHz). Unlike temperature profiling, humidity profiling offers very few
332 independent degrees of freedom (typically < 3), making it difficult for the MWR to resolve sharp vertical gradients often present
333 at the top of the convective boundary layer during the daytime. The structural deviation and underestimation are common
334 issues linked to the "smoothing" error inherent in passive radiometry, where sharp moisture inversions are averaged out.
335 Furthermore, the persistent bias suggests potential uncertainties in the water vapour absorption models (spectroscopic
336 parameters) or non-representative training data used in the retrieval algorithm.

337

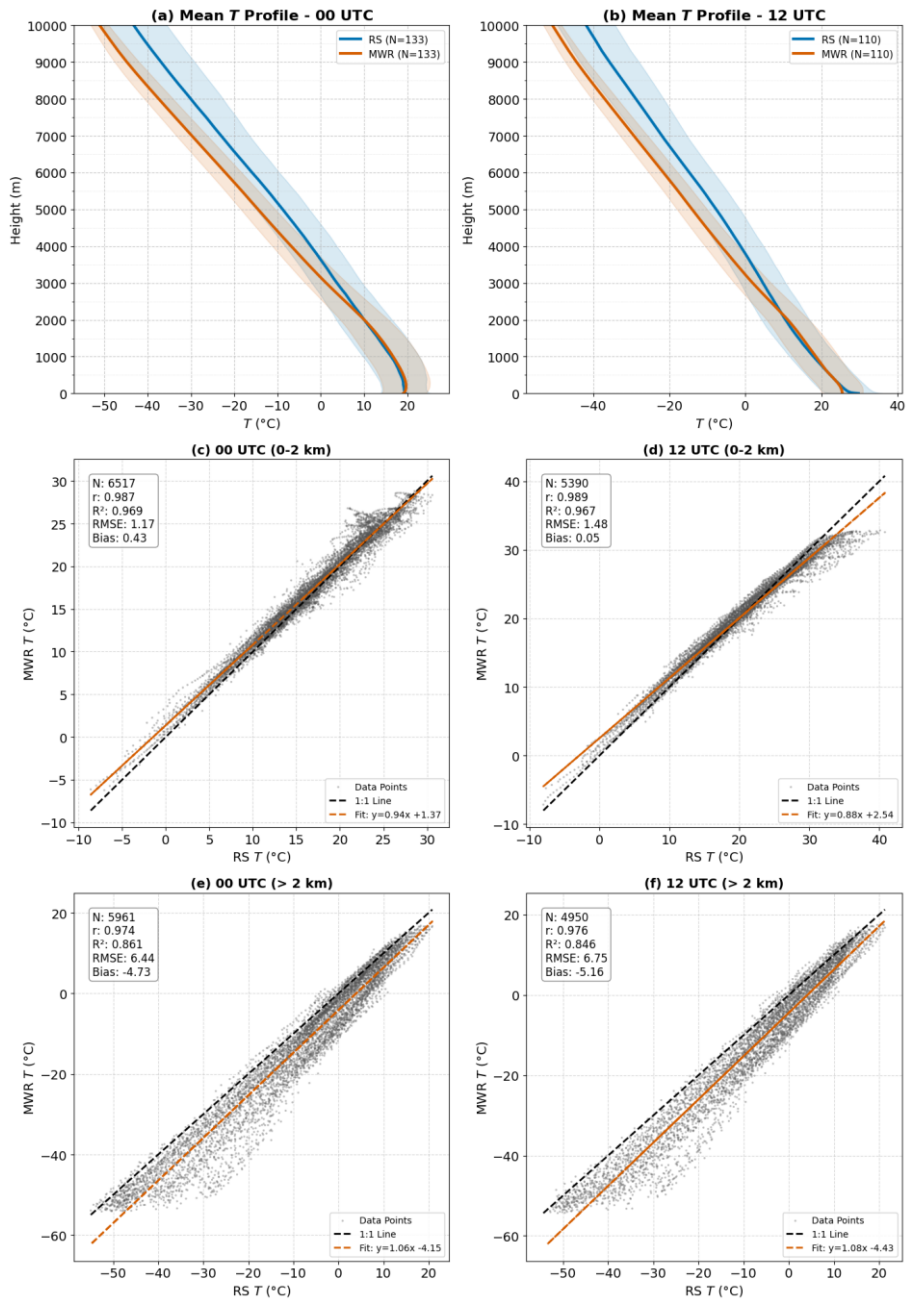
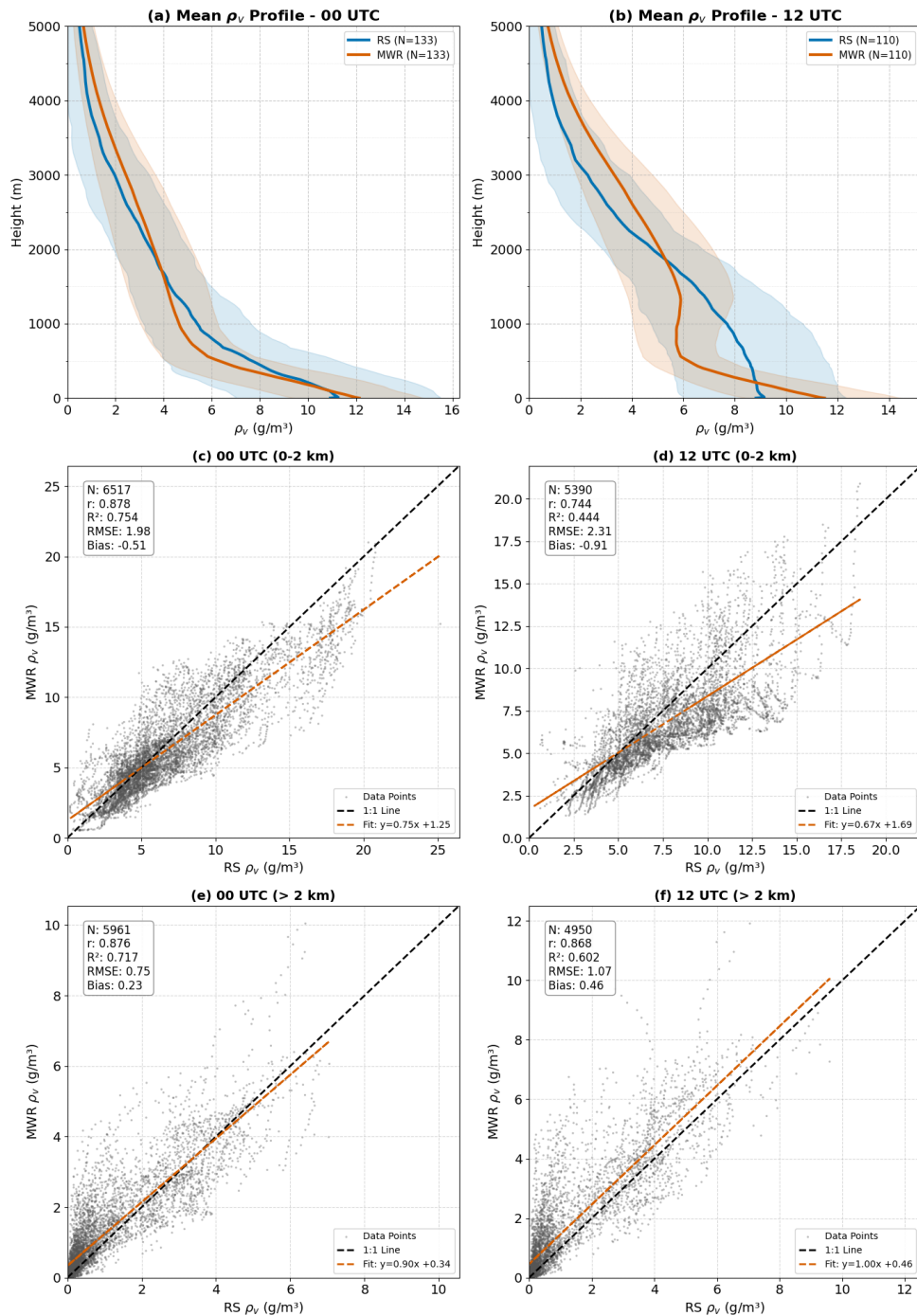


Figure 2. Comparison of radiosonde and microwave radiometer (MWR) temperature profiles: (a–b) Mean vertical temperature (T) profiles at 00 and 12 UTC with variability shading; (c–f) Scatter comparisons for the lower (0–2 km) and upper (>2 km) atmosphere at both times.

338
339
340
341

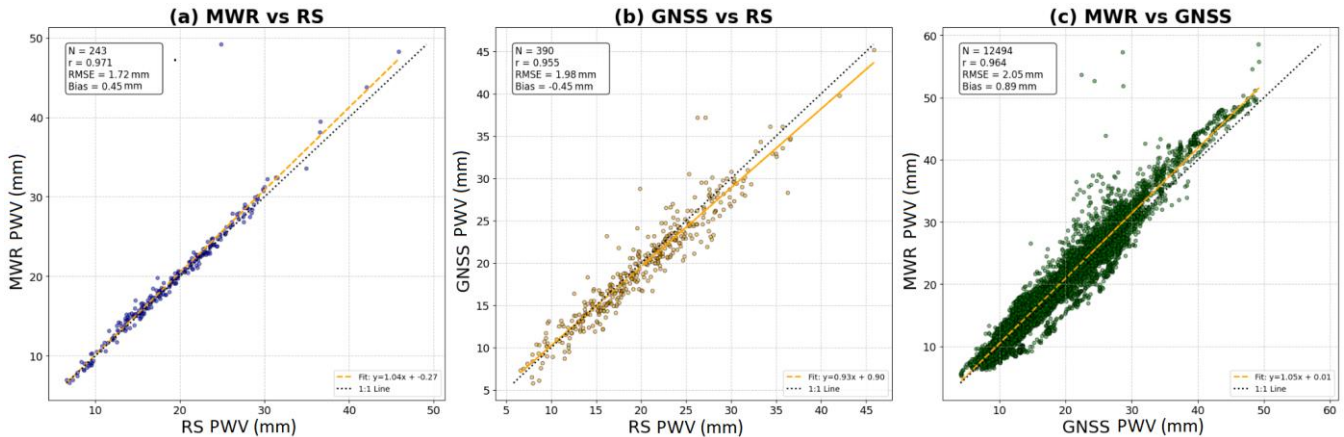


342 **Figure 3.** Comparison of radiosonde and microwave radiometer (MWR) absolute humidity (ρ_v) profiles: (a–b) Mean vertical ρ_v profiles at
 343 00 and 12 UTC with variability shading; (c–f) Scatter comparisons for the lower (0–2 km) and upper (>2 km) atmosphere at both times.
 344
 345

346 **3.2 Precipitable Water Vapour (PWV) and Scale Height (H_v) Validation**

347 Unlike vertical profiling, the MWR excels in measuring total column quantities. The comparison with RS yields an excellent
 348 correlation ($r=0.971$) and a low RMSE of 1.72 kg m^{-2} . This performance disparity—superior PWV versus degraded profiles—
 349 confirms that while the sensor cannot resolve vertical structural details due to smoothing error, the radiometric brightness
 350 temperature in the K-band remains strictly proportional to the total precipitable water mass. The GNSS-derived PWV shows
 351 a slight negative bias relative to RS (-0.45 kg m^{-2}), whereas it relative to the MWR exhibits a positive bias ($+0.45 \text{ kg m}^{-2}$). The
 352 cumulative offset observed in the MWR-GNSS intercomparison ($+0.89 \text{ kg m}^{-2}$) highlights the systematic differences in
 353 calibration and retrieval assumptions between active (GNSS) and passive (MWR) techniques. The GNSS underestimation is
 354 likely driven by errors in the T_m derived from the static HGPT2 model, a hypothesis further explored in Section 3.4. To further
 355 diagnose the structural limitations of the retrievals, we evaluated the water vapour H_v . While H_v is admittedly a single-
 356 parameter representation of the complex atmospheric moisture profile, it is a crucial parameter that provides a representative
 357 value for the rate at which water vapour decreases with altitude—a key factor in understanding atmospheric stability, cloud
 358 formation, and radiative transfer processes. In this study, it is utilized specifically as a diagnostic metric to quantify the vertical
 359 structural limitations of passive microwave remote sensing. The comparison of H_v calculated from RS and MWR profiles is
 360 shown in Fig. 5. Unlike the high-fidelity PWV retrievals, the MWR-derived scale height shows negligible correlation with RS
 361 observations ($r=0.25$, $R^2=-2.87$) and a massive systematic positive bias of 0.62 km . The histograms (Fig. 5b) further elucidate
 362 this discrepancy: while the RS scale heights follow a narrow, physically realistic distribution centered around a mean (μ) of
 363 1.51 km , the MWR distribution is artificially broad and shifted to significantly higher values ($\mu=2.13 \text{ km}$).

364



365

366

367

368

Figure 4. Intercomparison of precipitable water vapour (PWV) retrieved from Microwave Radiometer (MWR), GNSS, and Radiosonde observations. (a) MWR PWV versus radiosonde PWV, (b) GNSS PWV (derived using HGPT2 T_m) versus radiosonde PWV, and (c) MWR PWV versus GNSS PWV (derived using HGPT2 T_m).

369

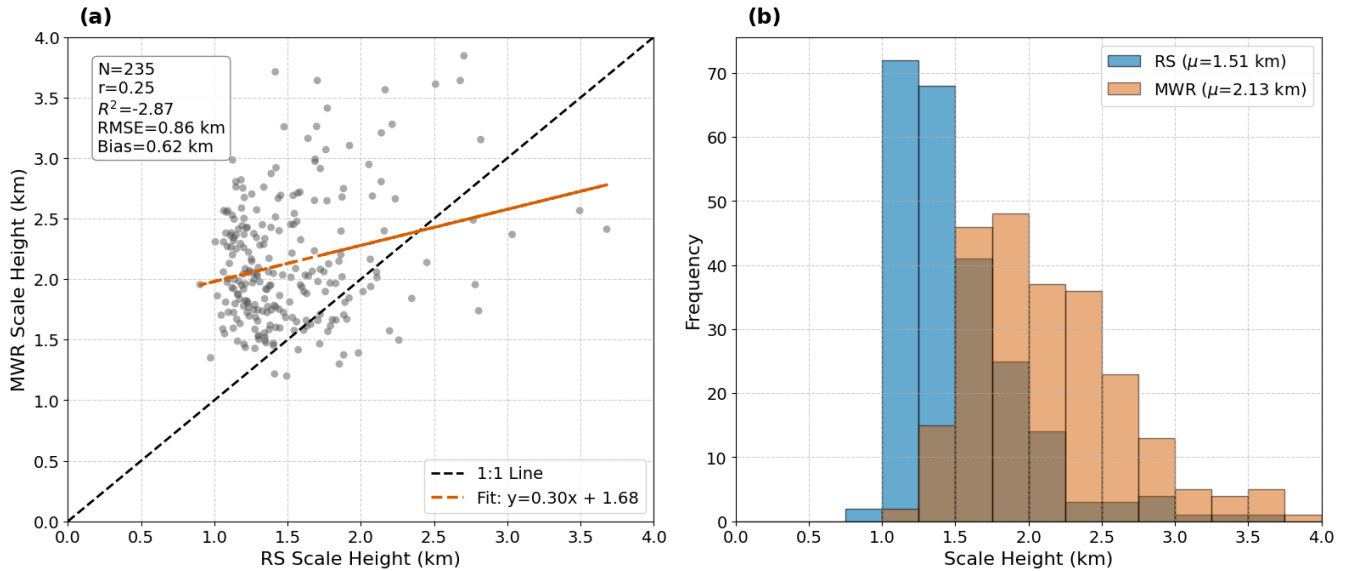
370

371

372

The large scatter and ambiguity in the MWR estimates—which completely dwarf the individual least-squares fit uncertainties of the exponential regression—are a direct consequence of the instrument's physical limitations. H_v is highly sensitive to the sharp vertical gradient of humidity at the top of the planetary boundary layer. However, the K-band channels (22–31 GHz) utilized for humidity profiling possess broad weighting functions, restricting the vertical degrees of freedom to

373 typically fewer than three. Because the MWR lacks the vertical resolution to capture sharp moisture inversions, the retrieval
 374 algorithm mathematically smears the moisture mass upward. This inherent 'smoothing error' artificially elongates the vertical
 375 moisture profile, effectively inflating the calculated e-folding depth. Therefore, the inclusion of this H_v analysis serves to
 376 transparently demonstrate a critical operational boundary: while the MWR is an excellent standard for PWV, it is significantly
 377 unreliable and mathematically unsuited for characterizing vertical moisture compactness. The significant deviations observed
 378 in these macroscopic retrieval products necessitate a deeper investigation into the intermediate thermodynamic variables
 379 driving the conversion process. Consequently, the isolated performance of the T_m is evaluated in Section 3.3, followed by the
 380 introduction of a post-retrieval MWR calibration scheme in Section 3.4 designed to mitigate these native biases.

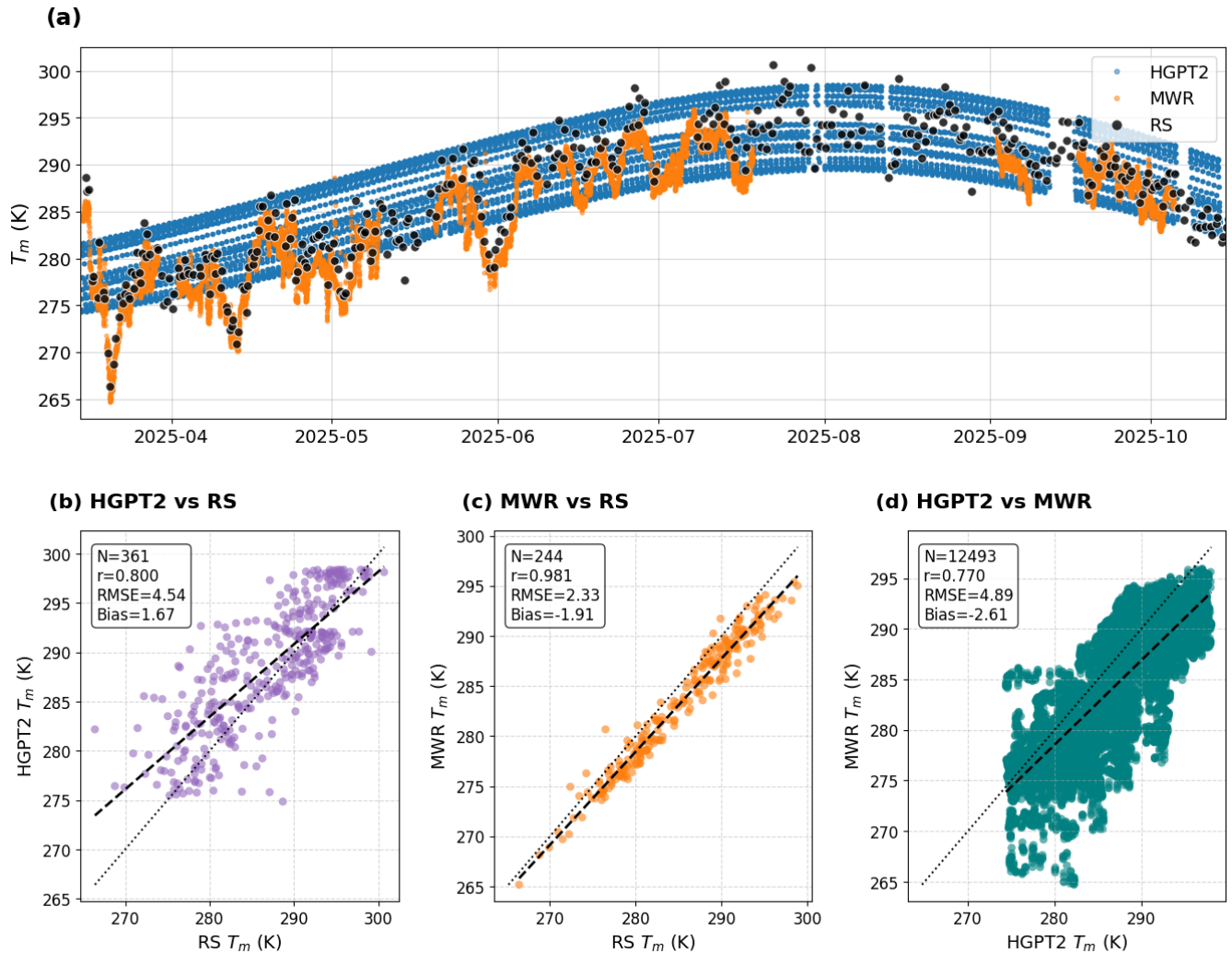


381 **Figure 5:** Comparison of scale height from radiosonde (RS) and microwave radiometer (MWR): (a) Scatter plot with 1:1 line and linear fit,
 382 including summary statistics; (b) Frequency distributions showing mean scale heights for RS and MWR.
 383
 384

385 3.3 Weighted Mean Temperature (T_m) Validation

386 The accurate estimation of the T_m is critical for converting GNSS-derived ZWD into PWV. The performance of T_m derived
 387 from the MWR and the empirical GPT2w model (HGPT2) was evaluated against RS measurements, which serve as the "ground
 388 truth." The results are presented in Fig. 6. The time series (Fig. 6a) illustrates the seasonal evolution of T_m from April to October
 389 2025. The Radiosonde observations (black dots) show significant variability, capturing synoptic-scale weather fluctuations.
 390 The MWR-derived T_m (orange dots) tracks these fluctuations with remarkable precision, overlaying the RS points almost
 391 perfectly. In stark contrast, the HGPT2 model (blue dots) provides a smooth, climatological curve. While it captures the general
 392 seasonal trend, it completely misses the day-to-day thermodynamic variability, often overestimating T_m during cooler transient
 393 events and underestimating it during warmer anomalies. The empirical model shows only moderate performance ($r=0.800$)
 394 with a substantial spread ($RMSE = 4.54$ K). A systematic positive bias of 1.67 K indicates that HGPT2 generally overestimates

395 the atmospheric temperature profile in this region. The scatter plot reveals a diffuse, "cloud-like" distribution, confirming its
396 inability to capture real-time atmospheric dynamics. The MWR demonstrates superior performance, achieving a near-perfect
397 correlation ($r=0.981$). The RMSE is significantly reduced to 2.33 K, which is nearly half the error of the empirical model.
398 Interestingly, the MWR exhibits a negative bias of -1.91 K, suggesting a systematic underestimation of T_m . Crucially, this bias
399 does not originate in the free troposphere, but rather in the planetary boundary layer (0–3 km). Since T_m is weighted by water
400 vapour pressure, this "cold bias" indicates the MWR is underestimating the intense near-surface heating or the sharp lapse
401 rates characteristic of the Nicosia environment. Despite this offset, the tight linearity indicates that MWR is an excellent source
402 for capturing real-time T_m variations. Comparing the large dataset of MWR against HGPT2 ($N=12,493$) confirms the
403 discrepancy between dynamic and static modeling. The correlation is lower ($r=0.770$) and the scatter is large (RMSE = 4.89
404 K), further proving that static empirical models are insufficient for high-precision GNSS meteorology compared to dynamic
405 radiometer measurements. While errors in ZTD estimation contribute significantly to the overall uncertainty budget, the
406 specific error introduced during the conversion from delay to water vapour is linearly dependent on the accuracy of T_m .
407 Assuming a given ZTD, a standard rule of thumb states that a 1 % relative error in T_m translates to roughly a 1 % relative error
408 in the resulting PWV. By switching from a static model (HGPT2, ~ 4.5 K error) to a dynamic sensor (MWR, ~ 2.3 K error),
409 the uncertainty in the GNSS water vapour product is effectively halved. This validates the "synergistic" approach of using
410 collocated MWR thermal data to process GNSS signals.



411
 412 **Figure 6.** Comparison of weighted mean temperature (T_m) derived from HGPT2, MWR, and Radiosonde (RS) during March–November
 413 2025. (a) Time series of T_m estimates from all three sources. (b–d) Scatter plots showing statistical comparisons between: (b) HGPT2 vs.
 414 RS, (c) MWR vs. RS, and (d) HGPT2 vs. MWR.

415

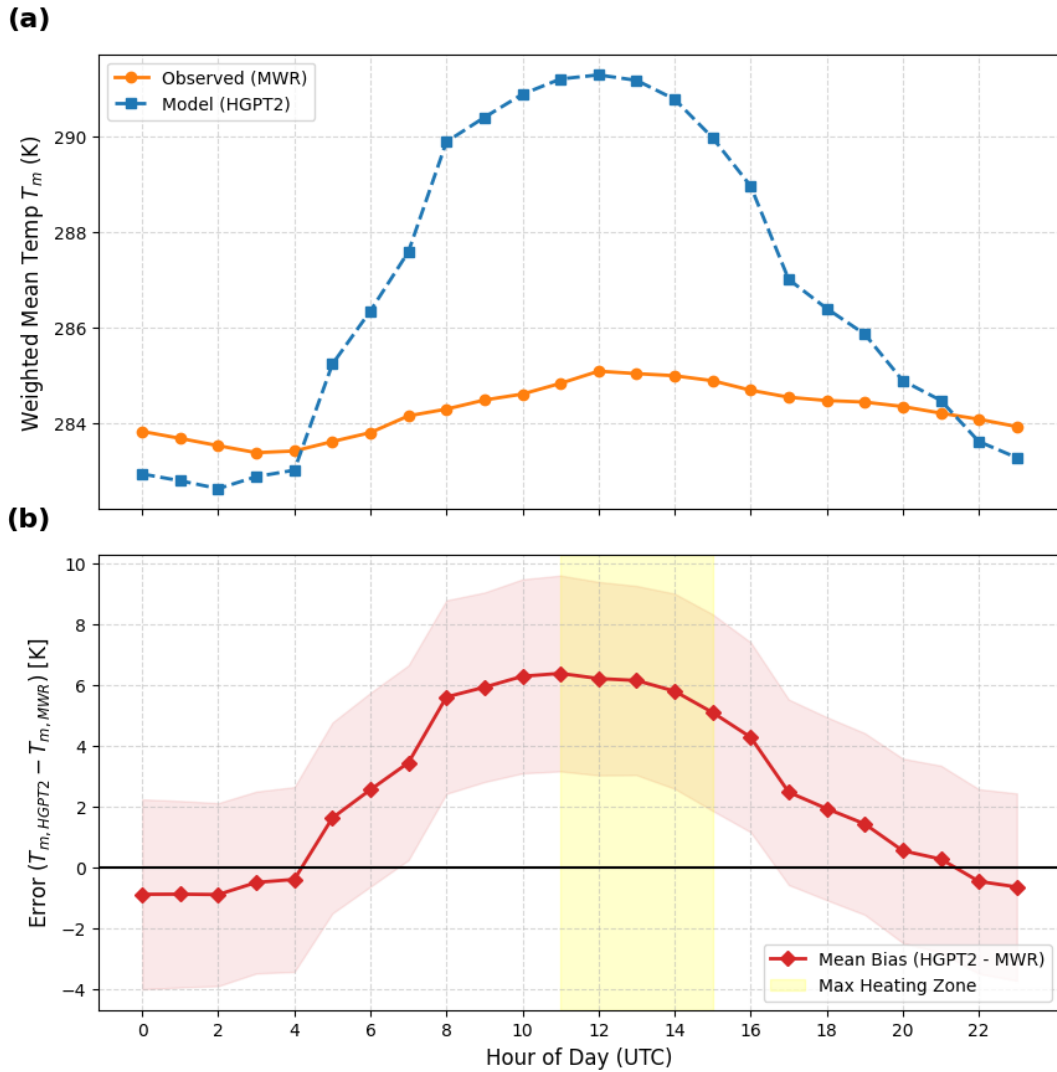
416 3.4 Diagnostic Analysis of Thermodynamic Conversion Uncertainty

417 3.4.1 Diurnal Bias Amplification in Static Models

418 To pinpoint the physical origin of the HGPT2 model's deficiency, a diurnal cycle analysis was performed (Fig. 7). While the
 419 previous statistical metrics indicated a general positive bias, the temporal breakdown in Fig. 7a reveals that this error is not
 420 uniform, but is driven by a fundamental misrepresentation of atmospheric thermodynamics. The MWR-derived T_m (orange
 421 line) exhibits a physically realistic, dampened diurnal amplitude of approximately 1.5 K. This stability reflects the high thermal

422 inertia of the tropospheric column, which does not heat rapidly in response to surface insolation. In stark contrast, the HGPT2
423 model (blue line) displays an exaggerated diurnal wave with an amplitude exceeding 8.5 K, peaking synchronously with solar
424 noon (12:00 UTC). As previously documented in the literature (Wang, 2005; Bock, 2021), deriving T_m via empirical regression
425 on surface temperature (T_s) is known to introduce spurious diurnal cycles. Our observations confirm this intrinsic limitation:
426 because the empirical model's periodic functions are overly sensitive to T_s , it assumes intense surface-level heating propagates
427 uniformly through the column, failing to capture the true thermodynamic decoupling between the turbulent planetary boundary
428 layer and the stable free troposphere. During the hours of peak solar insolation (11:00–14:00 UTC), the coastal environment
429 experiences active convective mixing and the onset of the sea breeze, which dramatically alters the vertical distribution of
430 water vapour. If the underlying reanalysis climatology fails to adequately resolve the sharp moisture capping inversion at the
431 top of the daytime planetary boundary layer (PBL), it will misrepresent the T_m weighting function. Specifically, if the model
432 traps too much moisture near the intensely heated surface—or fails to capture the thermodynamic decoupling between the
433 turbulent PBL and the stable free troposphere — the integral will disproportionately weight the hottest atmospheric layers.
434 This coupled temperature-humidity mechanism physically manifests as the severe diurnal bias peak effect observed in Fig. 7b,
435 where the systematic bias surges to over +6 K. This demonstrates that high-precision GNSS meteorology requires synergistic
436 MWR data to capture both the true thermal stability and the dynamic vertical moisture weighting of the atmosphere.

437



438
439
440
441
442

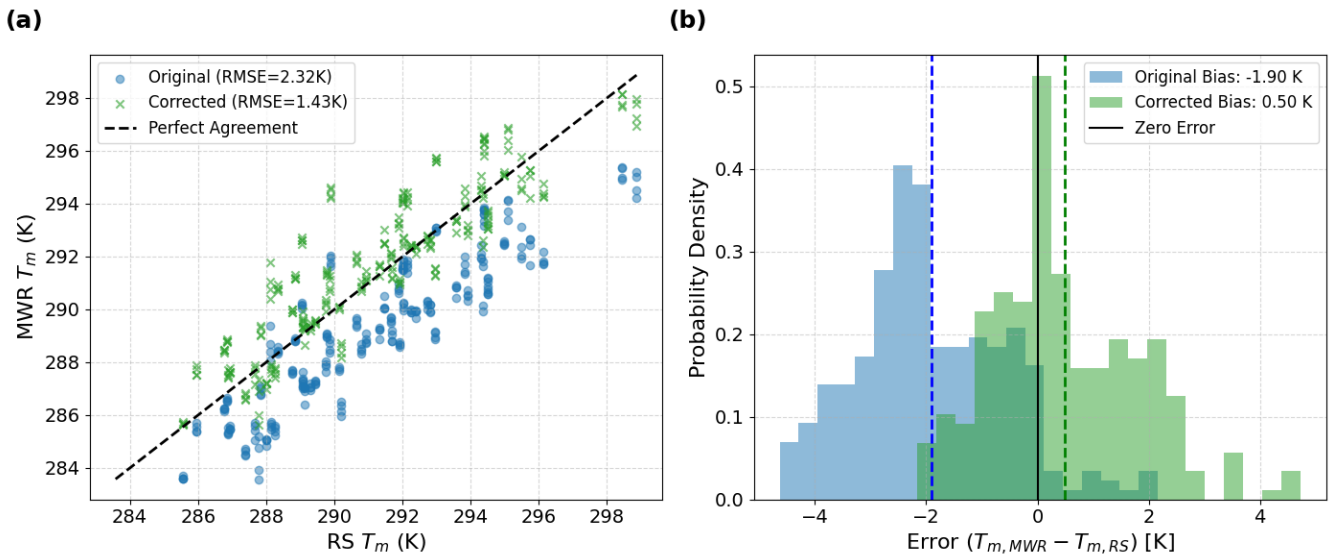
Figure 7. Diurnal variation of weighted mean atmospheric temperature T_m derived from microwave radiometer (MWR) observations and HGPT2 model simulations (top panel). The bottom panel shows the corresponding hourly mean bias ($T_{m,HGPT2} - T_{m,MWR}$), with shaded envelopes indicating variability. The yellow shaded region highlights the period of maximum daytime heating.

443 3.4.2 Calibration and Bias Correction of MWR T_m

444 Fig. 8 presents a statistical validation of the MWR derived T_m against co-located RS observations. The analysis highlights the
445 necessity and efficacy of a linear bias correction scheme to improve GNSS-PWV conversion accuracy. The scatter plot (Fig.
446 2a) reveals a distinct systematic deviation in the original MWR retrieval relative to the RS reference. The data points
447 consistently fall below the 1:1 identity line, indicating a negative bias in the raw MWR T_m product. The original RMSE is 2.32
448 K. This error is largely driven by the systematic offset rather than random scatter, as evidenced by the high linearity (R^2) of

449 the relationship. The thermodynamic profiles were retrieved using the manufacturer's standard Neural Network (NN)
450 algorithm, trained on Region historical RS data.

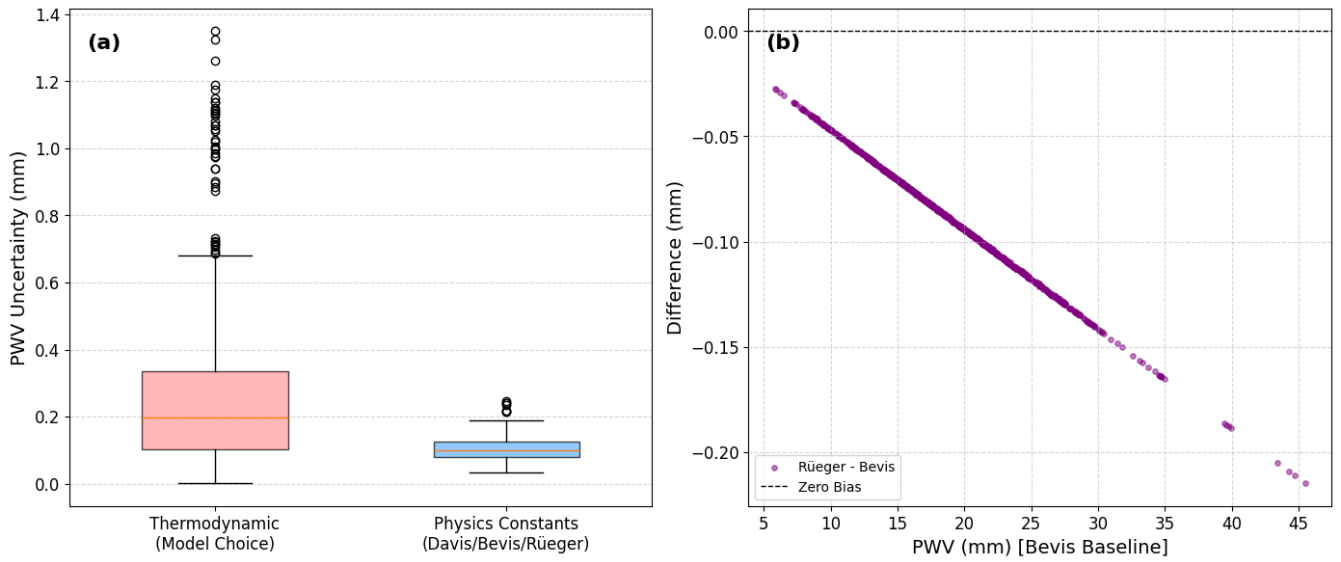
451 The Probability Density Function (PDF) of the errors ($T_{m,MWR} - T_{m,RS}$) in Fig. 8b clearly visualizes the bias shift. The pre-
452 correction distribution is non-Gaussian and shifted significantly to the negative domain, with a mean bias (μ) of -1.90 K. In
453 the context of GNSS meteorology, a T_m error of ≈ 2 K translates to a relative PWV error of approximately 0.7–1.0 %. For
454 climate monitoring, this represents a significant systematic dry bias. Applying the linear correction model (as formulated in
455 Section 2.2.1) successfully re-centers the error distribution. The post-correction bias is reduced to 0.50 K, and the histogram
456 aligns symmetrically around the zero-error line. The correction reduces the RMSE to 1.43 K, which is consistent with the
457 theoretical accuracy limit of ground-based radiometric profiling (typically 1–2 K). The remaining spread (width of the green
458 histogram) represents the random error component, likely attributable to instrumental noise and the imperfect spatiotemporal
459 matching between the instantaneous MWR zenith view and the drifting radiosonde balloon. The correction methodology
460 effectively removes the systematic instrumental bias without artificially compressing the natural variability of the atmosphere.
461 The reduction of RMSE by ~ 38 % (from 2.32 K to 1.43 K) confirms that site-specific calibration of T_m is a mandatory
462 processing step for generating climate-quality GNSS-PWV datasets.



463
464 **Figure 8.** Evaluation of weighted mean temperature T_m correction against Radiosonde (RS) observations. (a) scatter plots of original and
465 bias-corrected MWR-derived T_m versus RS T_m , with the dashed line indicating perfect agreement. (b) presents the probability density of
466 errors ($T_{m,MWR} - T_{m,RS}$) before and after correction, demonstrating a substantial reduction in cold bias and RMSE.
467

468 3.4.3 Uncertainty Budget Analysis

469



470 **Figure 9.** (a) PWV uncertainty attributed to thermodynamic assumptions and to the choice of refractivity constants. (b) Difference in GNSS-
 471 derived PWV resulting from the use of alternative refractivity constant formulations relative to Bevis et al. (1994).
 472

473
 474 In standard GNSS network processing, the largest source of PWV uncertainty is often the interpolation or modeling of
 475 surface pressure required to calculate the ZHD (Van Malderen et al., 2022). However, the CYGMEN observatory setup
 476 mitigates this spatial interpolation error by utilizing the co-located Vaisala WXT536 sensor, which has a stated pressure
 477 accuracy of ± 0.5 hPa. A 0.5 hPa pressure uncertainty propagates to approximately 1.15 mm of error in the ZHD. After applying
 478 the Π conversion factor, this restricts the pressure-induced PWV uncertainty to roughly ± 0.17 mm. Because this high-precision
 479 localized pressure data effectively minimizes ZHD uncertainty, the accuracy of the T_m parameterization emerges as the
 480 dominant remaining variable in the PWV error budget for this site.

481 It is important to note that the complete error budget for GNSS-derived PWV encompasses significant uncertainties
 482 originating from the ZTD estimation phase itself. These include geodetic errors such as satellite orbit and clock uncertainties,
 483 mapping function inaccuracies, and site-dependent electromagnetic effects like signal scattering and multipath. While these
 484 geodetic factors are critical, the following component-wise uncertainty analysis (Fig. 9) specifically isolates the errors
 485 introduced during the subsequent conversion step (Π). To decouple these retrieval contributions, two primary sources of
 486 uncertainty were isolated: the thermodynamic parameterization of T_m and the selection of atmospheric refractivity constants
 487 (k_2' , k_3). When decoupling these retrieval contributions, it is critical to distinguish between the statistical nature of the
 488 underlying error sources. As demonstrated by Healy (2011), uncertainties in the atmospheric refractivity constants (k_2' , k_3) act
 489 strictly as static systematic biases; selecting a different set of published constants permanently shifts the baseline of the Π by
 490 a fixed margin. Conversely, the uncertainty originating from the T_m parameterization is a dynamic, compound error. As
 491 highlighted by Wang et al. (2005) and Bock et al. (2021), empirical T_m models derived from surface temperatures often fail to

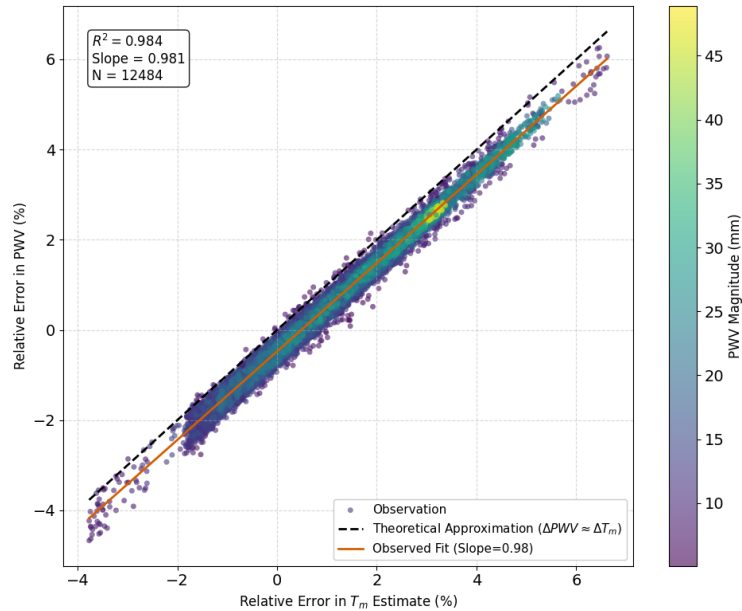
492 capture the true profile variance, introducing both a systematic bias (the model's mean regional offset) and a substantial random
493 error component (the statistical scatter, or RMSE, driven by real-time thermodynamic variability and diurnal decoupling).
494 While Fig. 9 juxtaposes these two distinct sources to illustrate their relative bounding magnitude on the final PWV product,
495 their significantly different statistical behaviors—static bias versus dynamic scatter—must be acknowledged. As illustrated in
496 Fig. 9(a), and explicitly evaluating the components of the conversion uncertainty framework established in Eq. (10), the
497 variance introduced by the T_m estimation strategy ($\sigma_{T_m}^2$) significantly outweighs the influence of the physical constants
498 ($\sigma_{k_2}^2, \sigma_{k_3}^2$). Feeding our empirically derived thermodynamic uncertainties into the partial derivative formulation defined in Eq.
499 (11) specifically, substituting the HGPT2 RMSE of 4.54 K versus the corrected MWR RMSE of 1.43 K as our σ_{T_m} values—
500 yields an isolated PWV retrieval error of approximately 1-2 mm due to stochastic thermodynamic variability. In contrast,
501 evaluating the exact mathematical limits of the refractivity coefficients ($\sigma_{k_2}, \sigma_{k_3}$) defined here as the maximum divergence
502 between the historical Davis et al. (1985), the standard Bevis et al. (1994), and the updated Rüeiger (2002) formulations—
503 results in an uncertainty an order of magnitude smaller. Fig. 9(b) further resolves the impact of the refractivity constants,
504 showing the differential bias between the oldest (Davis) and newest (Rüeiger) standards. The relationship is linear and
505 proportional to the total water vapour content, consistent with a scaling of the Π factor. While the transition to the Rüeiger
506 (2002) constants introduces a systematic positive shift, the magnitude of this correction (typically <0.2 mm for standard
507 loading) is negligible for synoptic meteorological applications compared to the noise induced by T_m errors. However, for long-
508 term climatological trend analysis where stability is paramount, consistent adherence to the Rüeiger (2002) standard is
509 recommended to eliminate this small, but persistent systematic bias. Overall, the correction of the T_m is 2.5 times more
510 important than selection of the constant.

511

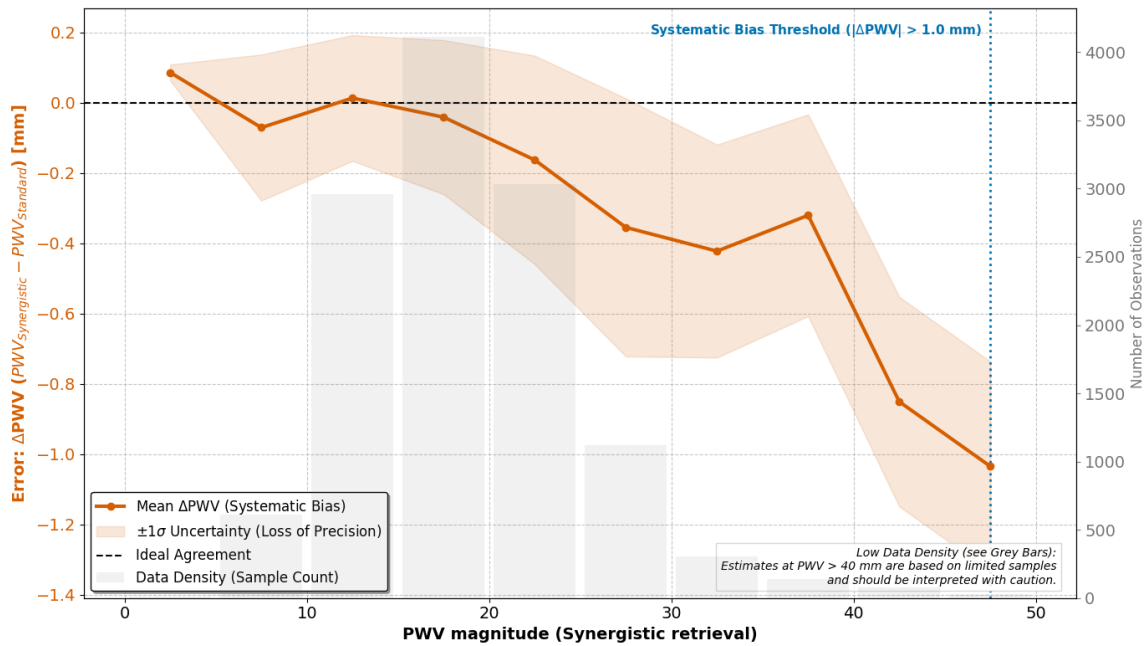
512 **3.5 Error Propagation and Synergistic Retrieval Assessment**

513 In this section, the PWV was derived using bias-corrected mean temperature (T_m) and constant values based on the study by
514 Rüeiger (2002), as mentioned in the Sect. 3.4. The impact of T_m errors on the final PWV product was analyzed to quantify the
515 benefits of the synergistic retrieval method. Fig. 10 visualizes the direct relationship between the relative error in T_m and the
516 resulting relative error in PWV. The plot reveals a strictly linear relationship ($R^2=0.984$) with a slope of 0.981. This confirms
517 the theoretical approximation that $(\Delta PWV/PWV) \approx (\Delta T_m/T_m)$. The color gradient indicates that this linear error propagation
518 holds true across all PWV magnitudes (from <10 mm to >45 mm). This implies that temperature errors propagate directly into
519 moisture errors regardless of the humidity level, making accurate T_m crucial at all times. Fig. 11 investigates the systematic
520 difference (ΔPWV) between the synergistic retrieval (using MWR T_m) and a standard retrieval (using empirical T_m) as a function
521 of moisture abundance (PWV magnitude). For drier conditions (PWV < 25 mm), the difference is minimal (near zero), and
522 the uncertainty (shaded region) is low. This suggests that for low humidity, the choice of T_m source is less critical. As
523 atmospheric moisture increases (> 25 mm), a significant negative bias emerges. The curve dips sharply, reaching nearly -1.0

524 mm at extreme humidity (45+ mm). The 'Systematic Bias Threshold' marker indicates that beyond 45 mm, the discrepancy
 525 exceeds 1.0 mm. The fact that the bias magnitude scales directly with total PWV provides physical confirmation that the error
 526 source is located in the boundary layer, where the bulk of the water vapour resides. The growing negative bias demonstrates
 527 that standard GNSS processing (using static models like HGPT2) systematically overestimates water vapour during extreme
 528 events compared to the more accurate synergistic method. Rather than extrapolating these localized errors to regional
 529 hydrological impacts, we emphasize the primary empirical observation: the systemic deviation of the standard empirical model
 530 scales proportionally with the magnitude of the PWV regime. Crucially, this systematic overestimation of moisture during
 531 extreme events is deeply intertwined with the diurnal cycle of the local atmosphere. This analysis quantifies the specific
 532 operational penalty of utilizing static climatological models in this region, demonstrating that HGPT2 incurs an PWV error
 533 exceeding 1.0 mm during severe thermodynamic events. As previously established (Fig. 7), the static HGPT2 model displays
 534 an exaggerated diurnal wave with an amplitude exceeding 8.5 K. Because the static model fails to account for the
 535 thermodynamic decoupling between the heated boundary layer and the cooler free troposphere during the day, this T_m error
 536 artificially inflates the amplitude of the GNSS-derived PWV diurnal cycle during peak solar insolation. By utilizing the
 537 synergistic retrieval approach, this spurious daytime moisture amplification is effectively mitigated. While further multi-site,
 538 long-term studies are required to assess the broader impacts on regional operational forecasting, our localized dataset clearly
 539 indicates that integrating real-time MWR thermal data successfully removes diurnal artifacts and reduces systematic
 540 measurement biases at this site.



541 **Figure 10.** Driver of model failure: Impact of weighted mean temperature (T_m) accuracy on PWV retrieval.
 542
 543
 544



545
546
547

Figure 11. Systematic breakdown and instability of the Standard GNSS model under extreme thermodynamic conditions.

548 **4 Discussions**

549 The results of this study necessitate a fundamental re-evaluation of how T_m parameterization errors are parameterized in GNSS
 550 meteorology, particularly within thermodynamically complex, semi-arid coastal environments like the Eastern Mediterranean.
 551 The pronounced failure of the static HGPT2 model to capture the diurnal T_m cycle reveals a structural limitation inherent to
 552 empirical modeling. The observed "diurnal bias peak" effect is not merely a statistical anomaly; it represents a physical
 553 disconnect. Static empirical models rely heavily on T_s , effectively assuming that intense surface-level heating propagates
 554 uniformly through the atmospheric column. This assumption critically breaks down during the daytime in the EM, where the
 555 turbulent planetary boundary layer (PBL) aggressively decouples from the stable free troposphere. Evidence for this severe
 556 decoupling is explicitly documented in the high-vertical-resolution RS profiles collected during the campaign. Because the
 557 passive MWR struggles to effectively capture this sharp boundary—a direct result of the broad weighting functions and
 558 degraded vertical resolution inherent to its K-band observations—the instrument exhibits a 'smoothing error' across the
 559 inversion layer. This structural limitation highlights exactly why applying a site-specific bias correction to the MWR's native
 560 output is a necessary prerequisite for precision GNSS meteorology. Furthermore, the failure of the reanalysis climatology to
 561 properly resolve the sharp moisture capping inversion during the onset of the daytime sea-breeze significantly corrupts the
 562 moisture-weighted T_m integral. Ground-based microwave radiometry overcomes this structural blindness by directly measuring
 563 the integrated thermal emissions of the column.

564 However, the performance of the MWR in this study highlights the duality of passive microwave remote sensing: it is highly
565 proficient at retrieving integral quantities but degrades severely when resolving differential or gradient-based parameters. The
566 successful reduction of the T_m RMSE via site-specific linear correction confirms that the MWR's K-band and V-band channels
567 effectively capture the true thermal inertia of the troposphere. The initial systematic cold bias observed aloft is a known artifact
568 of ill-posed neural network retrievals (Cimini et al., 2006; Löhnert and Maier, 2012). Because the vertical resolution of passive
569 microwave observations degrades rapidly with height, the retrievals become heavily constrained by historical training datasets
570 (the climatological prior), which often fail to capture localized, transition-season lapse rates in the free troposphere.
571 Conversely, the complete failure of the MWR to derive a physically realistic water vapour scale height (H_v) exposes the
572 "smoothing error" inherent to passive radiometry. Because the broad weighting functions of the K-band channels cannot
573 resolve sharp boundary layer moisture inversions, the retrieval algorithm mathematically smears the moisture mass upward.
574 This confirms that while MWR serves as a robust standard for total column mass, researchers must exercise extreme caution
575 when utilizing its smoothed profiles to characterize vertical moisture compactness.

576 While this study relies on a single-site, multi-month dataset, the physical mechanisms identified have broad relevance beyond
577 the Nicosia region. The Eastern Mediterranean serves as a highly representative climatic hotspot for semi-arid coastal
578 environments experiencing enhanced warming and intensified hydrological cycles. It is important to note that the specific
579 threshold of >45 mm identified here is characteristic of the climatological moisture capacity of the Eastern Mediterranean
580 during extreme summer anomalies. While the exact numerical value of this 'Systematic Bias Threshold' will vary
581 geographically depending on local atmospheric dynamics and latitude, the underlying physical principle remains universal:
582 empirical T_m models systematically degrade proportionally to the total atmospheric moisture mass during severe local
583 extremes. The core vulnerability exposed in this research—that static global models are structurally blind to sharp boundary
584 layer thermodynamic decoupling during peak insolation—is a fundamental physics problem, not a local anomaly. Therefore,
585 the proposed synergistic MWR-GNSS retrieval architecture provides a universally applicable solution for mitigating
586 systematic dry biases in any complex terrain or coastal environment globally. While the simple linear regression applied in
587 this study proved highly effective at correcting systematic T_m biases for operational GNSS conversions, there remains room
588 for algorithmic improvement. As the CYGMEN infrastructure accumulates a multi-year climatological database of high-
589 resolution radiosonde profiles, future work should focus on complementary Neural Network (NN) training. By retraining the
590 MWR retrieval algorithms using site-specific radiative transfer modeling rather than relying on the manufacturer's regional
591 historical priors, the native temperature and humidity profiles can be further optimized at the retrieval level.

592 Finally, our component-wise uncertainty analysis clarifies the error propagation chain in the GNSS-PWV conversion
593 process, shifting the paradigm of where optimization efforts should be focused. Historically, significant effort within the
594 geodetic community has been expended on refining atmospheric refractivity constants. However, we demonstrate that the error
595 induced by transitioning from the historical Davis et al. (1985) formulations to the modern Rüeiger (2002) constants is

596 practically negligible (<0.2 mm) for synoptic meteorological applications. The true "weak link" in the retrieval chain is
597 unequivocally the thermodynamic parameterization, which introduces errors an order of magnitude larger.

598

599 **5 Conclusion**

600 This study demonstrated that the accuracy of GNSS-derived Precipitable Water Vapour (PWV) in the Eastern Mediterranean
601 region, is significantly affected by the thermodynamic rigidity of static climatological models. By implementing a synergistic
602 retrieval strategy that couples GNSS delays with real-time ground-based microwave radiometry (MWR), we successfully
603 quantified and mitigated these limitations. The investigation yielded three primary methodological conclusions. First, we
604 established that standard empirical models (e.g., HGPT2) are structurally incapable of resolving the diurnal thermodynamic
605 decoupling between the boundary layer and free troposphere. This deficiency leads to severe systematic errors (the "diurnal
606 bias peak" effect) exceeding 6 K in weighted mean temperature (T_m) during peak solar insolation, which directly propagates
607 into a PWV bias >1.0 mm during extreme hygrometric events. Second, the MWR proved to be a superior source for T_m
608 parameterization errors, provided that site-specific calibration is applied. The development of a linear bias correction scheme
609 reduced the MWR T_m root-mean-square error from 2.32 K to 1.43 K. This correction substantially reduces the conversion-
610 related uncertainty in the GNSS water vapour product compared to standard climatological approaches. Third, the component-
611 wise sensitivity analysis confirmed that thermodynamic parameterization is a highly significant source of uncertainty that
612 exacerbates existing geodetic ZTD errors, outweighing uncertainties in refractive index constants by an order of magnitude.
613 Consequently, the proposed combined retrieval represents a highly valuable architectural upgrade for monitoring severe
614 weather in complex coastal environments like the Eastern Mediterranean. However, it must be acknowledged that there are
615 many sites worldwide where the deployment of microwave radiometers may not be justified. Given the high capital and
616 operational costs of radiometric hardware, the presence of other unmitigated geodetic uncertainties, and the adequate
617 performance of static T_m models in less thermodynamically complex regions, this synergistic approach is best reserved for
618 targeted deployments in highly vulnerable climatic hotspots.

619 For the climate-sensitive Eastern Mediterranean region, relying on static models for GNSS processing risks systematically
620 masking moisture trends during heatwaves and deep convection. We therefore recommend the operational integration of
621 collocated MWR observations into national GNSS processing chains. Where collocation is not feasible, future work should
622 focus on assimilating MWR-derived diurnal shape functions into static models to bridge the gap between climatology and
623 reality. This study establishes the "Corrected Synergistic Method" as a robust benchmark for generation of climate-quality
624 water vapour datasets in complex thermodynamic environments. From an operational perspective, relying exclusively on
625 MWRs for regional moisture monitoring is constrained by high capital costs, maintenance complexity, and signal degradation
626 during precipitation events. Conversely, GNSS networks provide highly cost-effective, dense, and all-weather monitoring

627 capabilities. The primary operational interest of this proposed methodology is the 'supersite' calibration strategy: utilizing a
628 centralized MWR to capture the true, real-time thermodynamic diurnal variations that static models like HGPT2 miss, and
629 subsequently assimilating these dynamic T_m corrections over a much wider, regional network of standard GNSS receivers.
630 This synergy allows forecasting centers to leverage the superior thermodynamic accuracy of a single MWR to drastically
631 improve the high-resolution, continuous PWV datasets generated by dense, low-cost GNSS infrastructure.

632

633 **Data availability**

634 The MWR and GNSS data used in this study are available from the CYGMEN project archive upon request. High resolution
635 Radiosonde data available from the Department of Meteorology (DoM), Cyprus. The ERA5 reanalysis data can be downloaded
636 from the Copernicus Climate Change Service (C3S) Climate Data Store.

637

638 **Author contributions**

639 ANP carried out the GNSS, MWR, and Radiosonde data processing, performed the synergistic PWV retrievals and error
640 diagnosis, and wrote the initial version of the paper. CO and HH conceptualized the study, acquired the funding and resources
641 for the CYGMEN infrastructure, and supervised the investigation. All authors discussed the results, edited, and proofread the
642 paper.

643

644 **Competing interests**

645 All authors declare that they have no conflict of interest.

646

647 **Acknowledgements**

648 We would like to express our sincere gratitude to the Cyprus Department of Meteorology (DoM) and in particular to Physicist
649 and Meteorology Officer Dr. Demetris Charalambous, for his invaluable guidance and for providing access to essential
650 resources at Athalassa observatory in Nicosia, Cyprus.

651

652 **Financial support**

653 The present study is funded by the Strategic Infrastructure project CYGMEN, which is implemented in the frames of Cohesion
654 Policy Programme “THALIA 2021-2027” and is co-funded by the European Union.

655

656 **References**

657 Askne, J. and Nordius, H.: Estimation of tropospheric delay for microwaves from surface weather data, *Radio Sci.*, 22, 379–
658 386, <https://doi.org/10.1029/RS0221003p00379>, 1987.

659 Bennartz, R. and Bauer, P.: Sensitivity of microwave radiances at 85–183 GHz to precipitating ice particles, *Radio Sci.*, 38,
660 8075, <https://doi.org/10.1029/2002RS002626>, 2003.

661 Bennett, G. V. and Jupp, A.: Operational assimilation of GPS zenith total delay observations into the Met Office numerical
662 weather prediction models, *Mon. Weather Rev.*, 140, 2706–2719, <https://doi.org/10.1175/MWR-D-11-00156.1>, 2012.

663 Bevis, M., Businger, S., Herring, T. A., Rocken, C., Anthes, R. A., and Ware, R. H.: GPS meteorology: Remote sensing of
664 atmospheric water vapor using the Global Positioning System, *J. Geophys. Res.*, 97, 15787–15801,
665 <https://doi.org/10.1029/92JD01517>, 1992.

666 Bevis, M., Businger, S., Chiswell, S., Herring, T. A., Anthes, R. A., Rocken, C., and Ware, R. H.: GPS meteorology: Mapping
667 zenith wet delays onto precipitable water, *J. Appl. Meteorol.*, 33, 379–386, [https://doi.org/10.1175/1520-0450\(1994\)033<0379:GMMZWD>2.0.CO;2](https://doi.org/10.1175/1520-0450(1994)033<0379:GMMZWD>2.0.CO;2), 1994.

669 Böhm, J., Möller, G., Schindelegger, M., Pain, G., and Weber, R.: Development of an improved empirical model for slant
670 delays in the troposphere (GPT2w), *GPS Solut.*, 19, 433–441, <https://doi.org/10.1007/s10291-014-0403-7>, 2015.

671 Bolton, D.: The computation of equivalent potential temperature, *Mon. Weather Rev.*, 108, 1046–1053,
672 [https://doi.org/10.1175/1520-0493\(1980\)108<1046:TCOEPT>2.0.CO;2](https://doi.org/10.1175/1520-0493(1980)108<1046:TCOEPT>2.0.CO;2) 1980.

673 Brenot, H., Neméghaire, J., Delobbe, L., Clerbaux, N., De Meutter, P., Deckmyn, A., Delcloo, A., Frappez, L., and Van
674 Roozendael, M.: Preliminary signs of the initiation of deep convection by GNSS, *Atmos. Chem. Phys.*, 13, 5425–5449,
675 <https://doi.org/10.5194/acp-13-5425-2013>, 2013.

676 Bock, O., Bosser, P., Flamant, C., Doerflinger, E., Jansen, F., Fages, R., Bony, S. and Schnitt, S.: Integrated water vapour
677 observations in the Caribbean arc from a network of ground-based GNSS receivers during EUREC 4 A. *Earth System Science*
678 *Data*, 13(5), pp.2407-2436. <https://doi.org/10.5194/essd-13-2407-2021>. 2021.

679 Cimini, D., Westwater, E. R., Gasiewski, A. J., Klein, M., Leuski, V. Y., and Dowlatshahi, S.: Thermodynamic atmospheric
680 profiling during the 2010 Winter Olympics using ground-based microwave radiometry, *IEEE T. Geosci. Remote*, 49, 4959–
681 4969, <https://doi.org/10.1109/TGRS.2011.2154337>, 2011.

682 Cimini, Domenico, Tim J. Hewison, Lorenz Martin, Jürgen Güldner, Catherine Gaffard, and Frank S. Marzano. "Temperature
683 and humidity profile retrievals from ground-based microwave radiometers during TUC." *Meteorologische Zeitschrift* 15, no.
684 1: 45-56. 2006.

685 Crewell, S. and Löhnert, U.: Accuracy of boundary layer temperature profiles retrieved with multifrequency multiangle
686 microwave radiometry, *IEEE T. Geosci. Remote*, 45, 2195–2201, doi: 10.1109/TGRS.2006.888434. 2007.

687 Douša, J. and Václavovic, P.: Real-time zenith tropospheric delays in support of numerical weather prediction applications,
688 *Adv. Space Res.*, 53, 1347–1358, <https://doi.org/10.1016/j.asr.2014.02.021>, 2014.

689 Davis, J. L., Herring, T. A., Shapiro, I. I., Rogers, A. E. E., and Elgered, G.: Geodesy by radio interferometry: Effects of
690 atmospheric modeling errors on estimates of baseline length, *Radio Sci.*, 20, 1593–1607,
691 <https://doi.org/10.1029/RS020i006p01593>, 1985.

692 Foth, A., Lochmann, M., Saavedra Garfias, P. and Kalesse-Los, H.: Determination of low-level temperature profiles from
693 microwave radiometer observations during rain. *Atmospheric Measurement Techniques*, 17(24), pp.7169-7181, 2024.

694 Gaffen, D. J.: Temporal inhomogeneities in radiosonde temperature records, *J. Geophys. Res.*, 99, 3667–3676,
695 <https://doi.org/10.1029/93JD03179>, 1994.

696 Giannadaki, D., Oikonomou, C., Haralambous, H., Tymvios, F., and Loizou, E.: Validation of precipitable water vapour
697 products using CyMETEO GNSS network in Cyprus, in: Eleventh International Conference on Remote Sensing and
698 Geoinformation of the Environment (RSCy2025), Vol. 13816, 397–409, SPIE, 2025.

699 Giorgi, F.: Climate change hot-spots, *Geophys. Res. Lett.*, 33, L08707, <https://doi.org/10.1029/2006GL025734>, 2006

700 Guerova, G., Jones, J., Douša, J., Dick, G., de Haan, S., Pottiaux, E., Bock, O., Pacione, R., Elgered, G., Vedel, H., and Bender,
701 M.: Review of the state of the art and future prospects of the ground-based GNSS meteorology in Europe, *Atmos. Meas. Tech.*,
702 9, 5385–5406, <https://doi.org/10.5194/amt-9-5385-2016>, 2016.

703 Held, I. M. and Soden, B. J.: Robust responses of the hydrological cycle to global warming, *J. Climate*, 19, 5686–5699,
704 <https://doi.org/10.1175/JCLI3990.1>, 2006.

- 705 Healy, S.B.: Refractivity coefficients used in the assimilation of GPS radio occultation measurements. *Journal of Geophysical*
706 *Research: Atmospheres*, 116(D1). <https://doi.org/10.1029/2010JD014013>. 2011.
- 707 Jiang, P., Ye, S., Chen, D., Liu, Y., and Xia, P.: Development of time-varying global gridded Ts-Tm model for precise GPS-
708 PWV retrieval, *Atmos. Meas. Tech.*, 12, 1233–1249, <https://doi.org/10.5194/amt-12-1233-2019>, 2019.
- 709 Jones, J., Guerova, G., Douša, J., Dick, G., de Haan, S., Pottiaux, E., Bock, O., Pacione, R., Elgered, G., Vedel, H., and Bender,
710 M.: Advanced GNSS Tropospheric Products for Monitoring Severe Weather Events and Climate, Springer, Cham,
711 <https://doi.org/10.1007/978-3-030-13901-8>, 2020.
- 712 Kiehl, J. T. and Trenberth, K. E.: Earth's annual global mean energy budget, *B. Am. Meteorol. Soc.*, 78, 197–208,
713 [https://doi.org/10.1175/1520-0477\(1997\)078<0197:EAGMEB>2.0.CO;2](https://doi.org/10.1175/1520-0477(1997)078<0197:EAGMEB>2.0.CO;2), 1997.
- 714 Lan, Z., Zhang, B., and Geng, T.: Establishment and analysis of global gridded Tm-Ts relationship model, *Geodesy and*
715 *Geodynamics*, 7, 101–107, <https://doi.org/10.1016/j.geog.2016.02.001>, 2016.
- 716 Lelieveld, J., Hadjinicolaou, P., Kostopoulou, E., Chenoweth, J., El Maayar, M., Giannakopoulos, C., Hannides, C., Lange,
717 M. A., Tanarhte, M., Tyrllis, E., and Xoplaki, E.: Climate change and impacts in the Eastern Mediterranean and the Middle
718 East, *Climatic Change*, 114, 667–687, <https://doi.org/10.1007/s10584-012-0418-4>, 2012.
- 719 Li, H., Wang, X., Wu, S., Zhang, K., Chen, X., Qiu, C., Zhang, Q., and Li, L.: Development of an improved model for
720 prediction of short-term heavy precipitation based on GNSS-derived PWV, *Remote Sens.*, 12, 4101,
721 <https://doi.org/10.3390/rs12244101>, 2020.
- 722 Löhnert, U. and Maier, O.: Operational profiling of temperature using ground-based microwave radiometry at Payerne:
723 Prospects and challenges, *Atmos. Meas. Tech.*, 5, 1121–1134, <https://doi.org/10.5194/amt-5-1121-2012>, 2012.
- 724 Mateus, P., Mendes, V. B., and Plecha, S. M.: HGPT2: an ERA5-based global model to estimate relative humidity, *Remote*
725 *Sens.*, 13, 2179, <https://doi.org/10.3390/rs13112179>, 2021.
- 726 Ning, T. and Elgered, G.: Intercomparison of MAX-DOAS vertical profile retrieval algorithms: studies on field data from the
727 CINDI-2 campaign, *Atmos. Meas. Tech.*, 14, 1–35, <https://doi.org/10.5194/amt-14-1-2021>, 2021.
- 728 Ning, Tong, J. Wang, G. Elgered, G. Dick, J. Wickert, Markus Bradke, M. Sommer, R. Querel, and D. Smale. "The uncertainty
729 of the atmospheric integrated water vapour estimated from GNSS observations." *Atmospheric Measurement Techniques* 9, no.
730 1. 79-92. doi:10.5194/amt-9-79-2016. 2016.

731 Pakkattil, A., Parde, A. N., Wagh, S., Lonkar, P., and Ghude, S. D.: Wintertime Intercomparison of Specific Humidity and
732 Temperature Profiles Measured by Microwave Radiometer (MWR), Radiosonde, and INSAT-3DR Sounder Over Delhi, India,
733 *J. Geophys. Res. Atmos.*, 130, e2025JD044462, <https://doi.org/10.1029/2025JD044462>, 2025.

734 Parde, A. N., Ghude, S. D., Prasad, V. S., Hari Prasad, K. B. R. R., Dhargar, N. G., Lonkar, P., and Rajeevan, M.: Influence
735 of ground-based microwave radiometer profile assimilation on fog genesis forecasts in the winter boundary layer of Northern
736 India, *J. Geophys. Res. Atmos.*, 130, e2024JD042224, <https://doi.org/10.1029/2024JD042224>, 2025.

737 Oikonomou, C., Tymvios, F., Pikridas, C., Bitharis, S., Balidakis, K., Michaelides, S., ... and Charalambous, D.: Tropospheric
738 delay performance for GNSS integrated water vapor estimation by using GPT2w model, ECMWF's IFS operational model and
739 in situ meteorological data, *Adv. Geosci.*, 45, 363–375, <https://doi.org/10.5194/adgeo-45-363-2018>, 2018.

740 Realini, E., Gatti, A., Reguzzoni, M., Sampietro, D., and Venuti, G.: GNSS-based precipitable water vapor retrieval for severe
741 weather monitoring: The 2014 Genoa flood case study, *Adv. Space Res.*, 53, 1–10, <https://doi.org/10.1016/j.asr.2014.02.015>,
742 2014.

743 Rüeiger, J. M.: Refractive index formulae for radio waves, in: Proceedings of the FIG XXII International Congress,
744 Washington, D.C., USA, 19–26 April 2002, 1–13, 2002.

745 Ross, R. J. and Elliott, W. P.: Tropospheric water vapor climatology and trends over North America: 1973–93, *J. Climate*, 9,
746 3561–3574, [https://doi.org/10.1175/1520-0442\(1996\)009<3561:TWVCAT>2.0.CO;2](https://doi.org/10.1175/1520-0442(1996)009<3561:TWVCAT>2.0.CO;2). 1996.

747 Saastamoinen, J.: Atmospheric correction for the troposphere and stratosphere in radio ranging satellites, in: The Use of
748 Artificial Satellites for Geodesy, *Geophys. Monogr. Ser.*, 15, 247–251, AGU, Washington, D.C.,
749 <https://doi.org/10.1029/GM015p0247>, 1972.

750 Soden, B. J. and Lanzante, J. R.: An assessment of satellite and radiosonde climatologies of upper-tropospheric water vapor,
751 *J. Climate*, 9, 1235–1250, [https://doi.org/10.1175/1520-0442\(1996\)009<1235:AAOSAR>2.0.CO;2](https://doi.org/10.1175/1520-0442(1996)009<1235:AAOSAR>2.0.CO;2), 1996.

752 Steinke, S., Ebell, K., Löhnert, U., Bozzo, A., Crewell, S., and Turner, D. D.: Assessment of small-scale integrated water
753 vapour variability during HOPE, *Atmos. Chem. Phys.*, 15, 2675–2692, <https://doi.org/10.5194/acp-15-2675-2015>, 2015.

754 Thayer, G. D.: An improved equation for the radio refractive index of air, *Radio Sci.*, 9, 803–807,
755 <https://doi.org/10.1029/RS009i010p00803>, 1974.

756 Trenberth, K. E., Fasullo, J., and Smith, L.: Trends and variability in column-integrated atmospheric water vapor, *Clim.*
757 *Dynam.*, 24, 741–758, <https://doi.org/10.1007/s00382-005-0017-4>, 2005.

758 Van Malderen, R., Brenot, H., Pottiaux, E., Beirle, S., Hermans, C., De Mazière, M., ... and Bruyninx, C.: A multi-site
759 intercomparison of integrated water vapour observations for climate change analysis, *Atmos. Meas. Tech.*, 7, 2487–2512,
760 <https://doi.org/10.5194/amt-7-2487-2014>, 2014.

761 Van Malderen, R., Pottiaux, E., Stankunavicius, G., Beirle, S., Wagner, T., Brenot, H., Bruyninx, C. and Jones, J.: Global
762 spatiotemporal variability of integrated water vapor derived from GPS, GOME/SCIAMACHY and ERA-Interim: Annual
763 cycle, frequency distribution and linear trends. *Remote Sensing*, 14(4), p.1050, <https://doi.org/10.3390/rs14041050>, 2022.

764 Van Baelen, J., Aubagnac, J.P. and Dabas, A.: Comparison of near–real time estimates of integrated water vapor derived with
765 GPS, radiosondes, and microwave radiometer. *Journal of Atmospheric and Oceanic Technology*, 22(2), pp.201-210, 2005.

766 Vaquero-Martínez, J., Antón, M., Ortiz de Galisteo, J. P., Cachorro, V. E., Wang, H., González-Abad, G., ... and Costa, M. J.:
767 Inter-comparison of integrated water vapor from ground-based GPS and satellite remote sensing at Mediterranean sites, *IEEE*
768 *J. Sel. Top. Appl.*, 11, 1718–1728, <https://doi.org/10.1109/JSTARS.2018.2812804>, 2018.

769 Ware, R., Cimini, D., Herzegh, P., Marzano, F., Vivekanandan, J. and Westwater, E.: Ground-based microwave radiometer
770 measurements during precipitation. In *8th Specialist Meeting on Microwave Radiometry* (pp. 24-27), 2004.

771 Wang, Junhong, Liangying Zhang, and Aiguo Dai. "Global estimates of water-vapor-weighted mean temperature of the
772 atmosphere for GPS applications." *Journal of Geophysical Research: Atmospheres* 110, no. D21. doi:10.1029/2005JD006215.
773 2005.

774 Yao, Y., Zhang, B., Yue, S., Xu, C., and Peng, W.: Analysis of the global Tm-Ts correlation and establishment of the latitude-
775 related linear model, *Chin. Sci. Bull.*, 59, 2340–2347, <https://doi.org/10.1007/s11434-014-0275-9>, 2014.

776 Ziskin Ziv, S., Yair, Y., Alpert, P., Uzan, L., and Reuveni, Y.: The diurnal variability of precipitable water vapor derived from
777 GPS tropospheric path delays over the Eastern Mediterranean, *Atmos. Res.*, 249, 105307,
778 <https://doi.org/10.1016/j.atmosres.2020.105307>, 2021.

779 Ziskin Ziv, S., Alpert, P., and Reuveni, Y.: Long-term variability and trends of precipitable water vapour derived from GPS
780 tropospheric path delays over the Eastern Mediterranean, *Int. J. Climatol.*, 41, 6433–6454, <https://doi.org/10.1002/joc.7205>,
781 2021.

782 Zittis, G., Hadjinicolaou, P., Klangidou, M., et al.: A multi-model, multi-scenario, and multi-domain analysis of regional
783 climate projections for the Mediterranean, *Reg. Environ. Change*, 19, 2621–2635, [https://doi.org/10.1007/s10113-019-01565-](https://doi.org/10.1007/s10113-019-01565-w)
784 [w](https://doi.org/10.1007/s10113-019-01565-w), 2019.